

The nexus between negative charge-transfer and reduced on-site Coulomb energy in correlated topological metals

A. R. Shelke,¹ C.-W. Chuang,² S. Hamamoto,³ M. Oura,³ M. Yoshimura,¹
N. Hiraoka,¹ C.-N. Kuo,^{4,5} C.-S. Lue,^{4,5} A. Fujimori,^{6,1,7} and A. Chainani¹

¹National Synchrotron Radiation Research Center, Hsinchu 300092, Taiwan

²Experimentelle Physik VII, Universität Würzburg, Am Hubland, D-97074 Würzburg, Germany

³RIKEN SPring-8 Center, Hyogo 679-5148, Japan

⁴Department of Physics, National Cheng Kung University, Tainan 70101, Taiwan

⁵Taiwan Consortium of Emergent Crystalline Materials,
National Science and Technology Council, Taipei, Taiwan

⁶Department of Physics, The University of Tokyo, 7-3-1 Hongo, Bunkyo-ku, Tokyo 113-0033, Japan

⁷Center for Quantum Technology, and Department of Physics,
National Tsing Hua University, Hsinchu 300044, Taiwan

(Dated: November 10, 2025)

The layered 3d transition metal dichalcogenides (TMDs) CoTe₂ and NiTe₂ are topological Dirac Type-II metals. Their *d*-bands do not exhibit the expected correlation-induced band narrowing seen in CoO and NiO. We address this conundrum by quantifying the on-site Coulomb energy U_{dd} via single-particle partial density of states and the two-hole correlation satellite using valence band resonant photoemission spectroscopy (PES), and obtain $U_{dd} = 3.0$ eV/3.7 eV for CoTe₂/NiTe₂. Charge-transfer (CT) cluster model simulations of the measured core-level PES and x-ray absorption spectra of CoTe₂ and CoO validate their contrasting electronic parameters: U_{dd} and CT energy Δ are (3.0 eV, -2.0 eV) for CoTe₂, and (5.0 eV, 4.0 eV) for CoO, respectively. The *d*-*p* hybridization strength T_{eg} for CoTe₂ < CoO, and indicates that the reduced U_{dd} in CoTe₂ is not due to T_{eg} . The increase in d^n -count ~ 1 by CT from ligand to Co site in CoTe₂ is due to a negative- Δ and reduced U_{dd} . Yet, only because $U_{dd} > |\Delta|$, CoTe₂ becomes a topological metal with *p*→*p* type lowest energy excitations. Similarly, we obtain a negative- Δ and reduced U_{dd} in NiTe₂ compared to NiO. The study reveals the nexus between negative- Δ and reduced U_{dd} required for setting up the electronic structure framework for achieving topological behavior via band inversion in correlated metals.

The 3d transition metal compounds (TMCs) show the largest variety of physical and chemical properties as 3d electrons manifest localized/delocalized as well as magnetic/non-magnetic character¹. Early studies^{2,3} considered TMC properties to originate purely from *d*-electrons, and ligand *p*-states were neglected assuming they were fully-filled bands lying far below the Fermi level (E_F). The work of Fujimori and Minami,⁴ and that of Zaanen, Sawatzky and Allen (ZSA)⁵ led to a paradigm shift by considering ligand *p*-electron states on an equal footing with *d*-electron states for describing the ground state character as well as excitations in TMCs. TMCs are now mainly characterized by the metal *d* on-site Coulomb energy U_{dd} and charge-transfer energy Δ between *d* and *p* states, both scaled by the *d*-*p* hybridization strength T .

The ZSA phase diagram⁵ classified TMCs into 4 categories: (i) Mott-Hubbard (MH) insulators with $U_{dd} < \Delta$ and a *d*-*d* gap between the lower (occupied) and upper (unoccupied) Hubbard bands (LHB and UHB, respectively), (ii) MH *d*-band metals, arising from LHB overlapping UHB, (iii) CT insulators with $U_{dd} > \Delta$ exhibiting a *p*-*d* gap between the occupied ligand band and UHB, and (iv) a *p*-type metal phase derived from a negative- Δ . Evidence of negative- Δ was first reported in insulating NaCuO₂ with a *p* - *p* gap⁶, and is now known in several TMCs like NdNiO₃⁷, AuTe₂⁸, TMS₂⁹, etc.

Extensive experimental and theoretical studies have shown that variation in electronic and magnetic properties of 3d TMCs originate from a large systematic variation in U_{dd} (~ 2 -8 eV for Ti-Cu^{1,3-5,10-12}) and ligand electronegativity which determines Δ in solids¹³. Here, as a measure of U_{dd} , we

include empirical U_E values¹⁰, U as used in density functional theory (DFT) calculations¹¹, and U_0 , the zero-frequency screened Coulomb interaction¹². In contrast, the 4*d* and 5*d* series of TMCs show much smaller values of U_{dd} (~ 1 -2 eV), and seemed less susceptible to cause property variations. In fact, until ~ 2005 , only late TM oxides were considered strongly correlated, while early 3*d* and the entire 4*d*, 5*d* series of TMCs were often said to be weakly correlated.

However, studies on early-3*d* and 4*d*, 5*d* TMCs have now shown that correlation effects can lead to Mott gaps in VTe₂¹⁴, Ba₂NaOsO₆¹⁵, Sr₂IrO₄¹⁶, Na₂IrO₃¹⁷, etc. Further, a Mott-insulator phase¹⁸ and superconductivity¹⁹ were discovered in twisted bilayer graphene with a very small effective Coulomb energy U_{eff} (~ 30 meV), but the narrow bandwidth ($W \sim 20$ meV) of the relevant Moiré band clarified its Mott-insulator behavior¹⁸. In contrast, recent angle-resolved PES (ARPES) studies on the late-3*d* TMDs 1*T*-CoTe₂ and 1*T*-NiTe₂ (hereafter, CoTe₂ and NiTe₂) have shown that they are topological Dirac Type-II metals with bulk spin-orbit split Te 5*p* bands crossing E_F ²⁰⁻²⁵. Both, CoTe₂ and NiTe₂ show weak Pauli paramagnetic-type susceptibility, and linear magnetoresistance upto 9 T applied field²⁶⁻²⁹. Surprisingly, they do not show evidence for the expected strong correlation effects like the very narrow *d*-band dispersions in CoO and NiO, which showed only 25% widths of the band dispersions obtained from DFT calculations³⁰.

In particular, band structure calculations of CoTe₂ showed band inversion between Te p_x+p_y and Te p_z orbitals just below and above E_F , leading to a bulk character Type-II

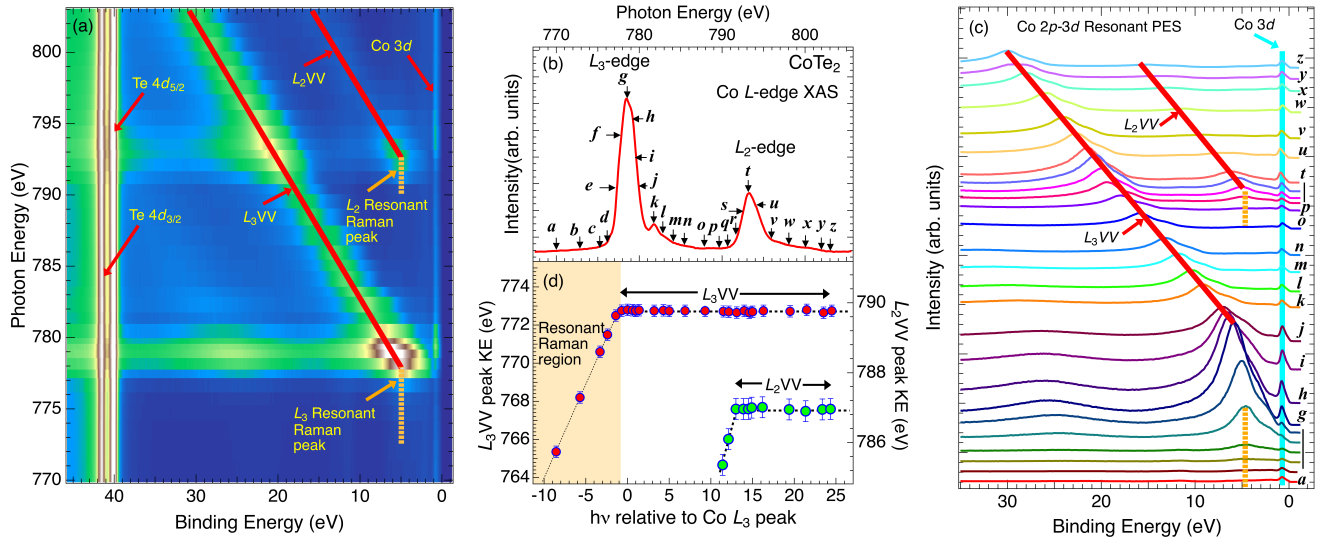


FIG. 1. (a). The Co $2p$ - $3d$ resonant-PES valence band intensity map plotted as a function of incident photon energies ($h\nu = 770$ - 803 eV) versus binding energy (BE = -1.2 to 45.8 eV). (b) The Co L_3 - and L_2 -edge XAS plotted as a function of $h\nu$ (top x-axis). (c) Valence band spectra (BE = -1.2 to 35.0 eV) measured at select $h\nu$ values (labelled a - z) across the L_3 - and L_2 -edges of Fig. 1(b). (d) The kinetic energy of the Resonant Raman - L_3VV Auger peak plotted as a function of $h\nu$ (top axis), and also relative to the XAS L_3 peak energy (bottom x-axis).

Dirac point lying ~ 0.9 eV above E_F ²⁰. Further, in combination with ARPES studies, it was shown that the Dirac points in surface states lie ~ 0.5 eV below E_F . However, the bandwidths obtained from DFT-GGA calculations without U were reduced by 70% to match experimental data, suggesting weak correlations²⁰. For NiTe_2 , independent studies for bulk NiTe_2 ²² and for 1 to 5 triatomic (Te-Ni-Te) layers²³, showed that DFT-GGA+ U calculations fail to improve agreement with experiments and concluded that calculations without U are most consistent with ARPES data. However, Fischer et al.³¹ calculated many-body effects within the GW approximation and found improvement in the Te $5p$ bands with an increase in Dirac carrier velocity compared to DFT results. Very recently, Bhatt et al.²⁵ used LDA+ U (with $U = 5$ eV) and concluded that a topological Ni $3d$ -Te $5p$ hybridized surface state lying ~ 1.5 eV below E_F gets shifted by 100 meV and better describes the ARPES data, but surprisingly, bulk electronic structure shows good agreement with LDA results and not with LDA+ U . Most importantly, the role of d -bands and electronic parameters of CoTe_2 and NiTe_2 , and specifically, the relation of Δ and U_{dd} with topological states and properties have not been addressed to date.

In order to solve this conundrum, we use resonant PES to quantify U_{dd} in CoTe_2 and NiTe_2 via measurements of the single-particle $3d$ partial density of states (PDOS) and the two-hole correlation satellite using the Cini-Sawatzky method³²⁻³⁵. The synthesis, structural characterization, spectroscopy details and core level measurements of CoTe_2 and NiTe_2 single crystals are described in the supplemental material (SM; Notes SN1, SN2)³⁶ and ref.³⁷. While ARPES studies corroborating the high-quality of CoTe_2 and NiTe_2 samples (from the same batches as present samples) have already been reported^{20,21}, angle-integrated off- and on-resonant va-

lence band PES ($h\nu = 700$ - 900 eV, 1.5 keV) and bulk sensitive core-level and valence band hard x-ray PES ($h\nu = 6.5$ keV) have not been reported to date.

Figure 1(a) shows the Co $2p$ - $3d$ resonant-PES valence band intensity map plotted as a function of incident photon energies ($h\nu = 770$ - 803 eV) versus binding energy (BE = -1.2 to 45.8 eV). In order to obtain the resonant-PES map, we first measure the Co L_3 - and L_2 -edge XAS shown in Fig. 1(b) as a function of $h\nu$ (top x-axis). This provides us the $h\nu$ range to obtain resonant-PES valence band spectra which constitute the map. In order to clarify the map features, Fig. 1(c) shows valence band spectra (BE = -1.2 to 35.0 eV) measured at select $h\nu$ values (labelled a - z) across the L_3 - and L_2 -edges of Fig. 1(b). The BEs were calibrated with respect to E_F of metallic CoTe_2 and the spectra are normalized to the shallow $4d$ core-level peaks (bright vertical lines at ~ 41 and 42 eV BEs) in the map. The map and Fig. 1(c) spectra show a small peak at 0.8 eV BE which gets enhanced on increasing $h\nu$ from a - g , and then gradually decreases for $h\nu = h$ - o across the L_3 -edge. On further increasing $h\nu$ from p - z across the L_2 -edge, the 0.8 eV feature undergoes another maxima at $h\nu = r$. This indicates that the 0.8 eV BE feature shows a Co $2p$ - $3d$ resonance, thus identifying the single-particle Co $3d$ PDOS. The 0.8 eV BE Co $3d$ PDOS feature (blue vertical line in Fig 1(c)) is also seen as a narrow vertical bright line in the map.

The main feature in the map is a high intensity diagonal (red full line) from the lower right to upper left corner. This high intensity diagonal originates from a peak feature at ~ 4.5 eV BE which shows an intensity increase for $h\nu = a$ - e , marked as an orange dashed line in the map and Fig. 1(c). As can be clearly seen in Fig. 1(c), the 4.5 eV BE peak systematically moves to higher BEs with a shift equal to the increase in $h\nu$ and corresponds to the Co L_3VV Auger feature. This is con-

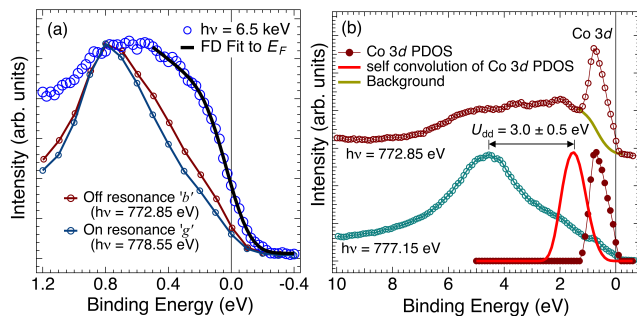


FIG. 2. (a) The CoTe₂ off-resonant ($h\nu = 772.85$ eV, maroon, \circ ; $h\nu = 6.5$ keV, blue, \circ) and on-resonant ($h\nu = 778.55$ eV, dark blue, \circ) near E_F spectra (normalized at 0.8 eV BE). (b) Co 3d PDOS (maroon, \bullet) obtained by subtracting an integral background (gray line) from off-resonant spectrum ($h\nu = 772.85$ eV (maroon, \circ)). The average U_{dd} is the energy between self-convoluted Co 3d PDOS peak (red line) and the Resonant Raman peak ($h\nu = 777.15$ eV; green, \circ), which becomes the LVV Auger peak.

firmed by plotting in Fig. 1(d) the kinetic energy of this peak as a function of $h\nu$ relative to the XAS L_3 peak energy (bottom x-axis). The actual incident $h\nu$ values are the same as top x-axis of Fig. 1(b). Thus, the peak at ~ 4.5 eV BE is a resonant Raman feature and becomes the correlation satellite with two holes in the final state, as is known for elemental metals^{38–40}. The map and Fig. 1(c) also show a weak broad feature at ~ 19.5 eV BE above the correlation satellite, which is due to plasmon excitations, as confirmed by core-level spectra (see SM; SN2, Figs. S1–S3). Further, for higher $h\nu = p$ -z, the map and Fig. 1(c) again show a weak resonance behavior for the Co L_2VV resonant Raman (orange dashed line) and the two hole correlation satellite Auger peak (red full line) of the 4.5 eV BE feature. The corresponding kinetic energy of this peak as a function of $h\nu$ is also plotted in Fig. 1(d) and confirms its two-hole final state Auger character.

In order to identify the Te 5p PDOS at and near E_F , in Fig. 2(a) we plot the off-resonant ($h\nu = 772.85$ eV, maroon, \circ) and on-resonant ($h\nu = 778.55$ eV, dark blue, \circ) near E_F CoTe₂ spectra after normalizing their peak intensities at 0.8 eV BE, and compare them with the CoTe₂ spectrum measured with $h\nu = 6.5$ keV (blue, \circ). At $h\nu = 6.5$ keV, the Te 5p states dominate the spectrum as the photo-ionization cross-section⁴¹ ratio of Te 5p:Co 3d is 9.47. The off- and on-resonant spectra show similar spectral shapes but the on-resonant spectrum gets narrowed, with suppressed relative spectral weight near E_F without a clear Fermi edge. This indicates that the Co 3d PDOS peak at 0.8 eV BE contributes weak spectral weight at E_F . In contrast, the CoTe₂ spectrum with $h\nu = 6.5$ keV shows a broader peak compared to the Co 3d PDOS peak. It extends all the way upto E_F and the leading edge matches the Fermi-Dirac (FD) fit, indicating that this feature is mainly derived from Te 5p states. This is consistent with ARPES experiments and comparison with DFT calculations which showed dominantly Te 5p states at and within 0.5 eV of E_F ²⁰. As we will show below (Fig. 3), this observation is also consistent with a negative- Δ in CoTe₂, but prior to that, we quantify U_{dd} by

applying the Cini-Sawatzky method^{32–35} to the Co 3d PDOS and the two-hole correlation satellite data.

Figure 2(b) shows the off-resonant spectrum obtained with $h\nu = 772.85$ eV before/after (maroon empty/full circles) subtracting an integral background (gray line) in order to separate out the single-particle Co 3d PDOS from the Te 5p states at higher BEs (see Fig. S5 and discussion in SM:SN3). The single-particle PDOS was then numerically self-convoluted to obtain the two hole spectrum (red line), and its peak energy represents the average two-hole energy without correlations. The two hole spectrum without correlations (red line) was then compared with the spectrum exhibiting the experimental two-hole correlation satellite spectrum in the resonant Raman region ($h\nu = 777.15$ eV; green empty circles). The energy separation between the peak in the two-hole spectrum without correlations and the peak of the experimental two-hole correlation satellite gives U_{dd} in the Cini-Sawatzky method. We obtain a value of $U_{dd} = 3.0$ eV, indicating that CoTe₂ is a moderately correlated material. We then used the obtained U_{dd} in CT cluster model calculations to simulate the Co 2p core-level PES and L-edge XAS in order to independently validate the U_{dd} value.

Figure 3(a,b) and (c,d) show experimentally measured Co 2p core-level PES and L-edge XAS spectra of CoTe₂ and CoO, respectively. A weak plasmon feature partly overlapping the Co $2p_{1/2}$ satellite of the CoTe₂ spectrum was removed after a fitting procedure (see SM; SN2, Fig. S4). The Co 2p PES spectrum of CoO was taken from ref⁴². The corresponding calculated spectra (full lines) are also overlaid on the experimental spectra (symbols). The calculated spectra were obtained from CT atomic multiplet cluster model calculations^{43,44}. We used the QUANTY code^{45–47} to calculate the spectra for a CoL₆ cluster (where, L is the ligand tellurium/oxygen atom) in an octahedral (O_h) local symmetry, as is known from the crystal structures of CoTe₂ and CoO. The calculations require the metal ion valency as an input and it is known that CoTe₂ and NiTe₂ exhibit a stable divalent state of Co²⁺ and Ni²⁺ with Te atoms in a dimerized (Te_2^{2-}) configuration with a reduced Te-Te distance along the c-axis, this being a generic feature of several late 3d, 4d and 5d TM tellurides crystallizing in the so called polymeric 1T-CdI₂ structure^{48,49} (see SN 1.1 for details). A recent XAS study of CoTe₂ showed that the Co L_3 -edge exhibits a Co²⁺ narrow main peak at $h\nu = 778.8$ eV⁵⁰. Our data of Fig. 3(b) also shows a very similar spectrum with the Co L_3 main peak at $h\nu = 778.8$ eV and confirms the divalent Co²⁺ (d^7) configuration in CoTe₂. On the other hand, the Co L_3 -edge XAS of Co²⁺ in CoO is known to exhibit a broad structured peak with the lowest multiplet prepeak at $h\nu = 778.1$ eV, a main peak multiplet at $h\nu = 780.0$ eV with a shoulder at $h\nu = 781$ eV^{51,52}, and our data is very consistent with these studies. For the Co 2p PES, the $2p_{3/2}$ main peak is at 777.9 eV for CoTe₂ and at 780.0 eV for CoO, consistent with reported values^{51,53–55}.

Based on the above, the Co²⁺ initial state for CoTe₂ and CoO is considered to be a linear combination of three basis states: $3d^7$, $3d^8\bar{L}^1$ and $3d^9\bar{L}^2$. The calculation was carried out for an octahedral ML₆ cluster and the details are described in SM:SN1. While CoTe₂ and NiTe₂ form in the 1T-CdI₂

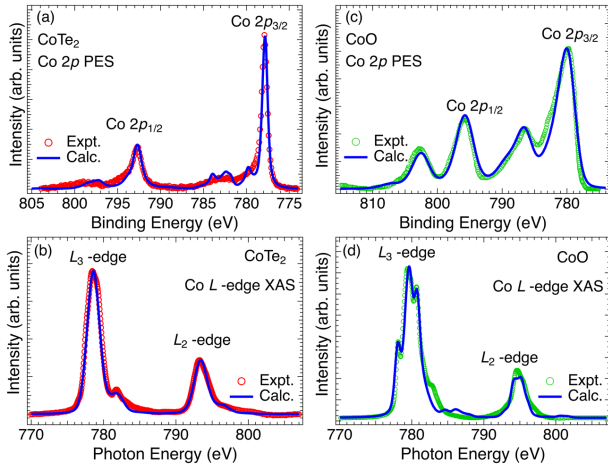


FIG. 3. (a) Co $2p$ PES core levels and (b) Co $L_{3,2}$ -edge XAS of CoTe₂ compared with charge transfer cluster model calculations. (c) Co $2p$ PES core levels and (d) Co $L_{3,2}$ -edge of CoO compared with charge transfer cluster model calculations.

TABLE I. Electronic parameters and d^n for materials using 3-basis state cluster model calculations.[†]from ref.⁶¹; *from ref.⁶

Parameter	CoTe ₂	CoO	NiTe ₂	NiO	CrTe [†]	NaCuO ₂ [*]
U_{dd} (eV)	3.0	5.0	3.7	7.0	3.5	7.0
Δ (eV)	-2.0	4.0	-2.8	6.0	-1.0	-2.0
T_{eg} (eV)	1.2	2.5	1.8	2.4	1.3	2.7
d^n count	8.14	7.21	9.04	8.15	4.98	8.81
U_{dd}/T_{eg}	2.5	2.0	2.1	2.9	2.7	2.6
$ \Delta /T_{eg}$	1.7	1.6	1.6	2.5	0.8	0.7

structure (SM:SN1), and CoO and NiO form in the rock salt structure, but they all share a similar local octahedral symmetry. It is noted that CoTe₂ and NiTe₂ actually exhibit a distortion from octahedral symmetry, but since the distortion is very small, they can be compared with the local octahedral symmetry of CoO and NiO. Using the experimentally obtained $U_{dd} = 3.0$ eV for CoTe₂ and a value of $U_{dd} = 5.0$ eV for CoO (from ref.⁵¹), we carried out an extensive set of calculations varying the values of Δ , T_{eg} , $T_{t2g}(=T_{eg}/2)$ and $10Dq$ to obtain calculated spectra very similar to the experimental spectra, as shown in Figs. 3(a-d). The same parameter set was used for calculating Co $2p$ core-level PES and L -edge XAS spectra of each material, and the main parameters are listed in Table I. The obtained parameters show that CoTe₂ is a negative- Δ system, while CoO is confirmed to be a positive- Δ system. While this is the first analysis of the CoTe₂ spectrum, the parameters for CoO are quite close to earlier analyses using a cluster model⁵¹, as well as a CT multiplet calculation combined with DMFT method⁵⁴(see SM Table IV for comparison of CoO parameters). The values of negative- Δ , U_{dd} , as well as the Slater parameters F_k and G_k for CoTe₂ and CoO were checked by systematic calculations to determine optimal parameters as detailed in SM:SN4, Figs. S6-S10. A negative- Δ is expected¹³ by the trend in the reduction of electronegativity from O→S→Se→Te in column 6A of the periodic table.

We also carried out analogous experiments and calcula-

tions for NiTe₂ and NiO,³⁷ and their main parameters are also listed in Table I. The parameters indicate a very similar behavior for NiTe₂ with a reduced $U_{dd}(= 3.7$ eV) from a Cini-Sawatzky analysis and a negative- $\Delta(= -2.8$ eV) from the calculations³⁷, while NiO is a positive- $\Delta(= 4.0$ eV) CT insulator with $U_{dd} = 7.0$ eV from Ni L -edge XAS calculations, as is known from earlier work⁵⁶. We have calculated the d -electron count in the ground state and the obtained values are 8.14 and 9.04 electrons for CoTe₂ and NiTe₂ (Table I). This indicates a dominant $3d^{n+1}\underline{L}^1$ contribution in the ground state (see SM;TableV) and is a signature of negative- Δ materials, as reported for insulating NaCuO₂⁶, metallic phase of the charge-density wave(CDW) rare-earth nickelates RNiO₃ which show metal-insulator transitions^{7,57-60}, ferromagnetic metal CrTe⁶¹, etc. It is noted that early cluster model calculations⁵⁷⁻⁵⁹ for the XAS of the metallic RNiO₃ used a small positive- Δ while the most recent study⁶⁰ used a negative- Δ , but all of them concluded a dominantly charge-transferred ground state.

It is important to note that the RNiO₃ materials with a formal valency of Ni³⁺ ions have a $3d^7$ electron configuration like Co²⁺ in CoTe₂. Several theoretical electronic structure calculations⁶²⁻⁶⁶ have been carried out to address the CDW transition mechanism and role of Coulomb correlations. In spite of the different theoretical methods(see SM:SN5), all of them agree that the Ni³⁺ $3d^7$ state gets stabilized to a dominantly $3d^8\underline{L}^1$ ground state in the high- T metallic phase, consistent with a negative- Δ . These studies concluded that a small or negative U_{eff} is qualitatively consistent with a negative- Δ . While CoTe₂ and NiTe₂ are not CDW systems, the present Cini-Sawatzky analyses results indicate moderate values of $U_{dd} = 3.0$ and 3.7 eV for CoTe₂ and NiTe₂, respectively, although it can actually provide even negative- U_{dd} values as was shown for TiSe₂ and CrSe₂^{67,68}. We have also checked that the occupied $3d$ -bands^{20-23,25} have a width $W_d < U_{dd}$ and hence, the cluster model is applicable to analyze CoTe₂ and NiTe₂. Table I also lists known parameters from two other negative- Δ materials, CrTe⁶¹ and NaCuO₂⁶, and all show a dominantly $3d^{n+1}\underline{L}^1$ ground state. Interestingly, Table I shows that for negative- Δ cases, while U_{dd} varies between 3.0 eV to 7.0 eV, the scaled Coulomb energy U_{dd}/T_{eg} and $|\Delta|/T_{eg}$ show small variation. It indicates that all the negative- Δ materials in Table I lie in a small region in the ZSA phase diagram. From Table I, it is clear that the d - p hybridization strength T_{eg} for CoTe₂ < CoO, related to the fact that the average Co-Te distance ($=2.565\text{\AA}$) is much larger than the average Co-O distance ($=2.13\text{\AA}$). Similarly, T_{eg} for NiTe₂ < NiO, because the Ni-Te distance ($=2.620\text{\AA}$) is larger than the Ni-O distance ($=2.09\text{\AA}$). This suggests that the reduction of U_{dd} in CoTe₂ and NiTe₂ compared to CoO and NiO is not caused by T_{eg} .

Next, we checked the relation of Δ and U_{dd} with d^n using CT cluster model calculations. Fig. 4(a) (red curves) shows the variation of d^n count vs. T_{eg} for different Δ values (keeping all other parameters fixed to optimal values for CoTe₂). The plots show that for Co²⁺, starting with $d^n = 7$ for $T_{eg} = 0$, we obtain a sharp increase of ~ 1 electron to $d^n \sim 8$ for the smallest considered finite $T_{eg} = 5$ meV, for all negative Δ , and also upto a small positive $\Delta \leq \Delta_C = 0.25$ eV. This indicates a spontaneous charge transfer takes place due to an effective negative- Δ to

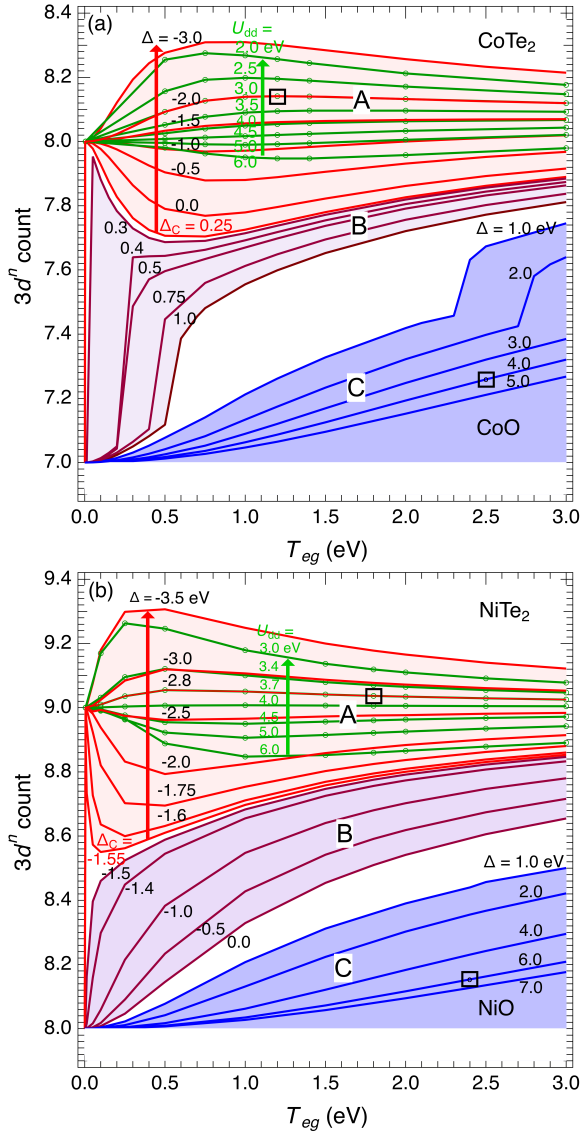


FIG. 4. Plots of d^n -count vs. T_{eg} for selected values of Δ and U_{dd} : (a) CoTe₂ and CoO (b) NiTe₂ and NiO, identify regions of effective negative- Δ (A) and effective positive- Δ (B, C). Squares (□) indicate optimal values which reproduce experimental spectra (Fig. 3).

form the dominantly $3d^{n+1}\underline{L}^1$ ground state for small $T_{eg} = 5$ meV. For optimal parameters ($\Delta = -2.0$ eV and $T_{eg} = 1.2$ eV) corresponding to spectra shown in Figs. 3(a,b), we obtain $d^n = 8.14$ (black square in Fig. 4a). For $T_{eg} = 5$ meV (see SM; SN6, Fig. S8(a)), the spin magnetic moment m_S vs. Δ also exhibits a jump at Δ_C , while for optimal $T_{eg} = 1.2$ eV, m_S vs. Δ does not show a jump but a smooth variation across Δ_C . We then checked the variation of d^n count vs. T_{eg} for $U_{dd} = 2.0 - 6.0$ eV (red curves; all other parameters fixed to optimal values for CoTe₂). The results in Fig. 4a show that in region A (pink shade), an increase in d^n is obtained on reducing Δ (making it more negative; red arrow) or reducing U_{dd} (green arrow). This indicates that the relatively large CT from ligand to Co site in CoTe₂ originates from a combination of effective

negative- $\Delta \leq \Delta_C$ and reduced U_{dd} . The microscopic origin of the reduction of U_{dd} is the polarizability of the anions, which is larger for Te than oxygen anions since the polarizability is roughly proportional to the anion size⁶⁹. Further, for $\Delta > \Delta_C$ (region B; purple shade), the sharp jump in d^n for $T_{eg} = 5$ meV gets suppressed for higher T_{eg} in the form of a reduced jump, followed by a gradual change at higher T_{eg} .

For CoO, a similar plot (Fig. 4(a); region C; blue shade) starts with $d^n = 7$ for $T_{eg} = 0$, and shows a gradual increase with T_{eg} for typical values of positive- Δ . For small $T_{eg} = 5$ meV, m_S vs. Δ shows a nearly constant value (see SM; Fig. S8b). However, for $\Delta \leq 2.0$ eV, a small jump is observed in d^n vs. T_{eg} , at high T_{eg} values. We have checked that the reduced jumps in regions B and C are due to spin-state transitions, as expected from cluster model calculations (see SM; Fig. S8c).

A very similar behavior with regions A and B for d^n vs. T_{eg} on varying Δ and U_{dd} is shown in Fig. 4(b), with a critical $\Delta_C = -1.55$ eV for the case of NiTe₂. Also, like CoO, a region C is obtained with positive- Δ for the case of NiO. Additional details for NiTe₂ and NiO are discussed in SM:SN6 and ref.³⁷. We have confirmed that Δ_C for CoTe₂ and NiTe₂ correspond to attaining an effective negative Δ (see SM:SN6, Fig. S9), defined as the energy difference between the lowest multiplet of d^n and $d^{n+1}\underline{L}^1$ states^{70–72}, i.e. a material attains a genuine negative- Δ state for $\Delta \leq \Delta_C$, when the lowest multiplet of the $d^{n+1}\underline{L}^1$ state becomes more negative than the lowest multiplet of the d^n state (see SM:SN6). Fig. 4 highlights regions of effective negative- Δ (A) and effective positive- Δ (B, C).

Finally, while U_{dd} gets reduced by $\sim 40\%/50\%$ compared to CoO/NiO, it is still larger than $|\Delta|$. It turns out that the reduced values of $U_{dd} = 3.0$ eV/3.7 eV for CoTe₂/NiTe₂ are just right, not too large and not too small. If U_{dd} was too small, CoTe₂ and NiTe₂ would have become d -band Mott-Hubbard systems in the ZSA picture, as shown schematically in Fig. 5(a). In contrast, if U_{dd} was too large, they would likely become positive- Δ materials like CoO and NiO (see Fig. 5(b)). But for the moderate U_{dd} as obtained for CoTe₂ from our experimental results and data analysis, it results in an appropriate $U_{dd} > |\Delta_{eff}|$ condition which allows Te p -band states to exhibit an effective negative- Δ with E_F positioned within the Te- p band states (see Fig. 5(c)). This results in a correlated metal with a narrow Co $3d$ band centered at 0.8 eV BE below E_F (Fig. 2), and simultaneously facilitates band inversion between Te $p_x + p_y$ and Te p_z orbitals just below and above E_F ²⁰. Thus, the ligand Te $5p$ states are sandwiched between the occupied and unoccupied $3d$ states in CoTe₂ (as well as in NiTe₂³⁷) and exhibit $p \rightarrow p$ -type lowest energy excitations. This picture fits well with Te $5p$ character bands at and near E_F seen in ARPES of CoTe₂²⁰ and NiTe₂^{21–23,25}. Further, as discussed in the introduction, band structure calculations for CoTe₂²⁰ showed that the bulk character Type-II Dirac point lies ~ 0.9 eV above E_F , and in combination with ARPES studies, it was shown that the Dirac points in surface states lie ~ 0.5 eV below E_F . Thus, while the Dirac points are somewhat away from E_F , an appropriate modification of the topological states via bandwidth-control or doping on the transition metal-site or ligand-site can lead to tuning a Dirac point closer to E_F and help to achieve robust topological transport properties.

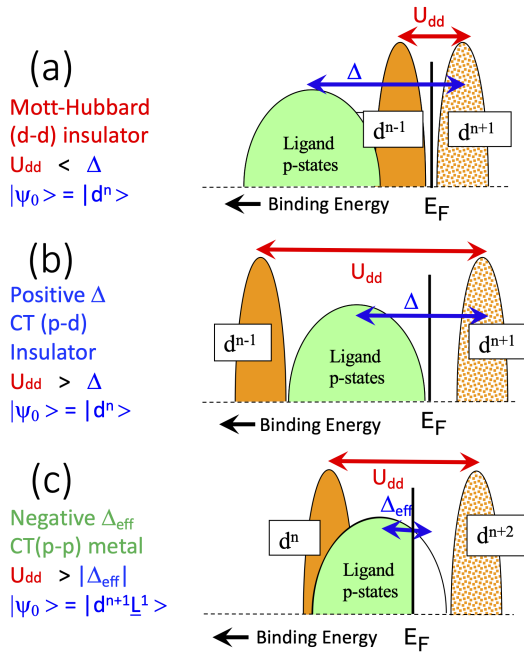


FIG. 5. Schematic electronic structure of materials representing: (a) a Mott-Hubbard insulator with $U_{dd} < \Delta$. A further reduction of U_{dd} would result in a Mott-Hubbard metal if the lower(occupied) and upper(unoccupied) Hubbard d -bands overlap. (b) a positive- Δ charge-transfer insulator with $U_{dd} > \Delta$ and $p \rightarrow d$ type lowest energy excitations (c) an effective negative- Δ metal with $U_{dd} > |\Delta_{eff}|$ and E_F positioned within the ligand- p band states, facilitating band inversion with $p \rightarrow p$ -type lowest energy excitations to make it a correlated topological metal. Note that for Mott-Hubbard and positive- Δ materials, the ground state $|\psi_0\rangle$ has a dominantly $|d^n\rangle$ character, while for an effective negative- Δ material, $|\psi_0\rangle$ has a dominantly $|d^{n+1}\underline{L}^1\rangle$ character, where \underline{L}^1 is a hole in the ligand p band.

In conclusion, we could quantify U_{dd} , Δ and T_{eg} in the topological metals CoTe_2 and NiTe_2 . The results show a negative- Δ for CoTe_2 and NiTe_2 , compared to a positive- Δ for the CT insulators CoO and NiO . The weaker T_{eg} in CoTe_2 and NiTe_2 compared to CoO and NiO , respectively, rules out T_{eg} as a cause of U_{dd} reduction. The obtained increase in charge-transfer is attributed to negative- Δ and a reduced U_{dd} . However, only because $U_{dd} > |\Delta|$, CoTe_2 and NiTe_2 become topological metals with $p \rightarrow p$ type lowest energy excitations. The study reveals the nexus between negative- Δ and reduced U_{dd} with E_F positioned within the Te- p band states. This results in a correlated metal and simultaneously facilitates band inversion between Te $p_x + p_y$ and Te p_z orbitals for achieving topological behavior in correlated metals.

This work was supported by the National Science and Technology Council(NSTC) of Taiwan under Grant Nos. NSTC 113-2112-M-006-009-MY2 (CNK), 110-2124-M-006-006-MY3 (CSL), 112-2124-M-006-009 (CSL), 113-2112-M-007-033 (AF), 112-2112-M-213-029(AC) and 114-2112-M-213-021(AC). AF acknowledges support from the Yushan Fellow Program under the Ministry of Education of Taiwan and Grant No. JP22K03535 from Japan Society for the Promotion of Science(JSPS). ARS thanks the National Science and Technology Council(NSTC) of Taiwan for a post-doctoral fellowship under Grant No. NSTC 114-2811-M-213-006.

- ¹ M. Imada, A. Fujimori, and Y. Tokura, Metal-insulator transitions, *Rev. Mod. Phys.* 70, 1039 (1998).
- ² D. Adler, Mechanisms for Metal-Nonmetal Transitions in Transition-Metal Oxides and Sulfides, *Rev. Mod. Phys.* 40, 714 (1968).
- ³ L. F. Mattheiss, Electronic Structure of the 3d Transition-Metal Monoxides I and II, *Phys. Rev. B* 5, 290 (1972); *Phys. Rev. B* 5, 306 (1972).
- ⁴ A. Fujimori and F. Minami, Valence-band photoemission and optical absorption in nickel compounds, *Phys. Rev. B* 30, 957(1984).
- ⁵ J. Zaanen, G. Sawatzky, and J. Allen, Band gaps and electronic structure of transition-metal compounds, *Phys. Rev. Lett.* 55, 418 (1985).
- ⁶ T. Mizokawa, H. Namatame, A. Fujimori, K. Akeyama, H. Kondo, H. Kuroda, and N. Kosugi, *Phys. Rev. Lett.* 67, 1638 (1991).
- ⁷ V. Bisogni, S. Catalano, R. J. Green, M. Gibert, Y. Huang, R. Scherwitzl, V. N. Strocov, P. Zubko, S. Balandeh, J.-M. Triscone, G. Sawatzky, and T. Schmitt, Ground-state oxygen holes and the metal-insulator transition in the negative charge-transfer rare-earth nickelates, *Nat. Commun.* 7, 13017 (2016).
- ⁸ S. V. Streltsov, V. V. Roizen, A. V. Ushakov, A. R. Oganov, and D. I. Khomskii, Old puzzle of incommensurate crystal structure of

calaverite AuTe_2 and predicted stability of novel AuTe compound, *Proc. Natl Acad. Sci. USA* 115, 9945 (2018).

- ⁹ A. Z. Laila, T. L. Nguyen, R. Furui, A. Shelke, F.-H. Chang, H.-J. Lin, C.-T. Chen, S. Hamamoto, A. Fujimori, T. Mizokawa, and others, Comparative study of a high-entropy metal disulfide and its parent compounds using x-ray absorption spectroscopy, *Phys. Rev. B* 109, 195129 (2024).
- ¹⁰ J. Zaanen and G.A. Sawatzky, Systematics in band gaps and optical spectra of 3D transition metal compounds, *Journal of Solid State Chemistry* 88, 8 (1990).
- ¹¹ V. I. Anisimov, J. Zaanen, and O. K. Andersen, Band theory and Mott insulators: Hubbard U instead of Stoner I, *Phys. Rev. B* 44, 943 (1991).
- ¹² M. Casula, Ph. Werner, L. Vaugier, F. Aryasetiawan, T. Miyake, A. J. Millis, and S. Biermann, Low-Energy Models for Correlated Materials: Bandwidth Renormalization from Coulombic Screening, *Phys. Rev. Lett.* 109, 126408 (2012).
- ¹³ G.A. Sawatzky and R. Green, in *Quantum Materials: Experiments and Theory* (Verlag des Forschungszentrum Jülich, Jülich, 2016), ed. E. Pavarini, E. Koch, J. van den Brink, and G. Sawatzky, Chap. 1, p. 19.
- ¹⁴ W.-M. Zhao, W Ding, Q.-W. Wang, Y.-X. Meng, L. Zhu, Z.-Y.

- Jia, W. Zhu, and S.-C. Li, Observation of Electronic Strong Correlation in VTe_2 - $2\sqrt{3} \times 2\sqrt{3}$ Monolayer, *Phys. Rev. Lett.* 131, 086501 (2023).
- 15 A. S. Erickson, S. Misra, G. J. Miller, R. R. Gupta, Z. Schlesinger, W. A. Harrison, J. M. Kim, and I. R. Fisher, *Phys. Rev. Lett.* 99, 016404 (2007).
 - 16 B. J. Kim, H. Jin, S. J. Moon, J.-Y. Kim, B.-G. Park, C. S. Leem, Yu. Jaeeun, T. W. Noh, C. Kim, S.-J. Oh, J.-H. Park, V. Durairaj, G. Cao, and E. Rotenberg, *Phys. Rev. Lett.* 101, 076402 (2008).
 - 17 Y. Singh and P. Gegenwart, Antiferromagnetic Mott insulating state in single crystals of the honeycomb lattice material Na_2IrO_3 , *Phys. Rev. B* 82, 064412 (2010).
 - 18 Y. Cao, et al. Correlated insulator behaviour at half-filling in magic-angle graphene superlattices. *Nature* 556, 80 (2018).
 - 19 Y. Cao, et al. Unconventional superconductivity in magic-angle graphene superlattices. *Nature* 556, 43 (2018).
 - 20 A. Chakraborty, J. Fujii, C.-N. Kuo, C. S. Lue, A. Politano, I. Vobornik, and A. Agarwal, Observation of highly anisotropic bulk dispersion and spin-polarized topological surface states in CoTe_2 , *Phys. Rev. B* 107, 085406 (2023).
 - 21 B. Ghosh, D. Mondal, C.-N. Kuo, C. S. Lue, J. Nayak, J. Fujii, I. Vobornik, A. Politano, and A. Agarwal, Observation of bulk states and spin-polarized topological surface states in transition metal dichalcogenide dirac semimetal candidate NiTe_2 , *Phys. Rev. B* 100, 195134 (2019).
 - 22 S. Mukherjee, S. W. Jung, S. F. Weber, C. Xu, D. Qian, X. Xu, P. K. Biswas, T. K. Kim, L. C. Chapon, M. D. Watson, J. B. Neaton and C. Cacho *Scientific Reports* 10, 12957 (2020).
 - 23 J. A. Hlevyack, L.-Y. Feng, M.-K. Lin, R. A. B. Villaos, R.-Y. Liu, P. Chen, Y. Li, S.-K. Mo, F.-C. Chuang, and T.-C. Chiang, Dimensional crossover and band topology evolution in ultrathin semimetallic NiTe_2 films, *npj 2D mater. appl* 5, 40 (2021).
 - 24 M. Nurmamat, S. V. Ereameev, X. Wang, T. Yoshikawa, T. Kono, M. Kakoki, T. Muro, Q. Jiang, Z. Sun, M. Ye, and A. Kimura, Bulk Dirac cone and highly anisotropic electronic structure of NiTe_2 , *Phys. Rev. B* 104, 155133 (2021).
 - 25 N. Bhatt, A. Ali, D. Sharma, S. Bansal, M. Mandal, R. P. Singh and R. S. Singh, Strongly correlated topological surface states in the type-II Dirac semimetal NiTe_2 , *Phys. Rev. B* 111, 245157 (2025).
 - 26 X. Wang, Z. Zhou, P. Zhang, S. Zhang, Y. Ma, W. Yang, H. Wang, B. Li, L. Meng, H. Jiang, S. Cui, P. Zhai, J. Xiao, W. Liu, X. Zou, L. Bao, and Y. Gong, Thickness-Controlled Synthesis of CoX_2 ($X = \text{S}, \text{Se}, \text{and Te}$) Single Crystalline 2D Layers with Linear Magnetoresistance and High Conductivity, *Chem. Mater.* 32, 2321 (2020).
 - 27 J. Shi, Y. Huan, M. Xiao, M. Hong, X. Zhao, Y. Gao, F. Cui, P. Yang, S. J. Pennycook, J. Zhao, and Y. Zhang, Two-Dimensional Metallic NiTe_2 with Ultrahigh Environmental Stability, Conductivity, and Electrocatalytic Activity, *ACS Nano* 14, 9011 (2020).
 - 28 Q. Mao, Y. Zhang, Q. Chen, R. Li, X. Geng, J. Yang, H. Hao, M. Fang, Metallicity and Paramagnetism of Single-Crystalline NiTe and NiTe_2 *Phys. Stat. Solidi B* 257, 1000224 (2020).
 - 29 C. Xu, B. Li, W. Jiao, W. Zhou, B. Qian, R. Sankar, N. D. Zhigadlo, Y. Qi, D. Qian, F.-C. Chou, and X. Xu, Topological Type-II Dirac fermions approaching the Fermi level in a transition metal dichalcogenide NiTe_2 , *Chem. Mater.* 30, 4823 (2018).
 - 30 Z.-X. Shen, C. K. Shih, O. Jepsen, W. E. Spicer, I. Lindau, and J. W. Allen, Aspects of the correlation effects, antiferromagnetic order, and translational symmetry of the electronic structure of NiO and CoO , *Phys. Rev. Lett.* 64, 2442 (1990).
 - 31 F. Fischer, A. Torche, M. Prada, and G. Bester, GW effects on the topology of Type-II Dirac cones in NiTe_2 , PtSe_2 , and PtTe_2 , *Phys. Rev. B* 110, 165146 (2024).
 - 32 M. Cini, Density of states of two interacting holes in a solid, *Solid State Commun.* 20, 605 (1976).
 - 33 M. Cini, Two hole resonances in the XVV auger spectra of solids, *Solid State Commun.* 24, 681 (1977).
 - 34 G. Sawatzky, Quasiatomic Auger spectra in narrow-band metals, *Phys. Rev. Lett.* 39, 504 (1977).
 - 35 M. Cini, Comment on Quasiatomic Auger spectra in narrow-band metals, *Phys. Rev. B* 17, 2788 (1978).
 - 36 See Supplemental Material at [URL will be inserted by publisher] for the synthesis, structural characterization, experimental and cluster calculation methods, supporting core level and off-resonant valence band spectroscopy data, and spectral calculations confirming the optimal electronic parameters.
 - 37 A complementary study on the experimental results for NiTe_2 and NiO is submitted to *Phys. Rev. B* as a regular article (available on arXiv at <http://arxiv.org/abs/2511.02245>).
 - 38 C. Guillot, Y. Ballu, J. Paigne, and J. Lecante K. P. Jain, P. Thiry, R. Pinchaux, Y. Petroff, and I.M. Falicov, Resonant Photoemission in Nickel Metal, *Phys. Rev. Lett.* 39, 1632 (1977).
 - 39 M. Weinelt, A. Nilsson, M. Magnuson, T. Wiell, N. Wassdahl, O. Karis, A. Föhlisch, N. Mårtensson, J. Stöhr, and M. Samant, Resonant photoemission at the 2p edges of Ni: Resonant raman and interference effects, *Phys. Rev. Lett.* 78, 967 (1997).
 - 40 Hüfner, S.-H. Yang, B. Mun, C. Fadley, J. Schäfer, E. Rotenberg, and S. Kevan, Observation of the two-hole satellite in Cr and Fe metal by resonant photoemission at the 2p absorption energy, *Phys. Rev. B* 61, 12582 (2000).
 - 41 M. Trzhaskovskaya and V. Yarzhevsky, Dirac-Fock photoionization parameters for HAXPES applications, *At. Data Nucl. Data Tables* 119, 99 (2018).
 - 42 A. Chainani, T. Yokoya, Y. Takata, K. Tamasaku, M. Taguchi, T. Shimojima, N. Kamakura, K. Horiba, S. Tsuda, S. Shin, D. Miwa, Y. Nishino, T. Ishikawa, M. Yabashi, K. Kobayashi, H. Namatame, M. Taniguchi, K. Takada, T. Sasaki, H. Sakurai, and E. Takayama-Muromachi, Bulk electronic structure of $\text{Na}_{0.35}\text{CoO}_2 \cdot 3\text{H}_2\text{O}$, *Phys. Rev B* 69, 180508(R)(2004).
 - 43 F. De Groot, X-ray absorption and dichroism of transition metals and their compounds, *J. Electron Spectros. Relat. Phenomena* 67, 529 (1994).
 - 44 F. de Groot and A. Kotani, *Core Level Spectroscopy of Solids* (CRC Press, Boca Raton, FL, 2008).
 - 45 M. W. Haverkort, M. Zwierzycki, and O. K. Andersen, Multiplet ligand-field theory using Wannier orbitals, *Phys. Rev. B - Condens. Matter Mater. Phys.* 85, 165113 (2012).
 - 46 Y. Lu, M. Höppner, O. Gunnarsson, and M. W. Haverkort, Efficient real-frequency solver for dynamical mean-field theory, *Phys. Rev. B* 90, 085102 (2014).
 - 47 M. W. Haverkort, G. Sangiovanni, P. Hansmann, A. Toschi, Y. Lu, and S. Macke, Bands, resonances, edge singularities and excitons in core level spectroscopy investigated within the dynamical mean-field theory, *EPL* 108, 57004 (2014).
 - 48 S. Jovic, R. Brec and J. Rouxel, Anionic Polymeric Bonds in Transition Metal Ditellurides, *Jl. Solid State Chem.* 96, 169 (1992).
 - 49 W. Bensch, W. Heid, M. Muhler, S. Jovic, R. Brec, and J. Rouxel, Anionic polymeric bonds in Nickel Ditelluride: crystal structure, and experimental and theoretical band structure, *J. Solid State Chem.* 121, 87 (1996).
 - 50 T.-H. Lu, C.-J. Chen, Y.-R. Lu, C.-L. Dong, and R.-S. Liu, Synergistic-effect-controlled CoTe_2 /carbon nanotube hybrid material for efficient water oxidation, *J. Phys. Chem. C* 120, 28093 (2016).
 - 51 J. van Elp, J.L. Wieland, H. Eskes, P. Kuiper, G.A. Sawatzky, F. M. F. de Groot, and T. S. Turner, *Phys. Rev. B* 44, 6090 (1991).
 - 52 J. Okamoto, A. Chainani, Z. Y. Chen, H. Y. Huang, A. Singh,

- T. Sasagawa, D. I. Khomskii, A. Fujimori, C. T. Chen, and D. J. Huang, Evolution of valence- and spin-specific local distortions in $\text{La}_{2-x}\text{Sr}_x\text{CoO}_4$, *Phys. Rev. B* 104, 054417 (2021).
- ⁵³ Z. Hu, L. Zhang, A. Chakraborty, G. D. Olimpio, J. Fujii, A. Ge, Y. Zhou, C. Liu, A. Agarwal, I. Vobornik and other, Terahertz nonlinear hall rectifiers based on spin-polarized topological electronic states in $1T\text{-CoTe}_2$, *Adv. Mater.* 35, 2209557 (2023).
- ⁵⁴ M. Ghiasi, A. Hariki, M. Winder, J. Kunes, A. Regoutz, T.-L. Lee, Y. Hu, J.-P. Rueff, and F. M. F. de Groot, *Phys. Rev. B* 100, 075146(2019).
- ⁵⁵ J. F. Moulder, W. F. Stickle, P. E. Sobol, and K. D. Bomben, *Handbook of X-ray Photoelectron Spectroscopy* (Perkin-Elmer Corporation, 1992).
- ⁵⁶ M. A. Veenendaal, D. Alders and G. A. Sawatzky, Influence of superexchange on Ni 2p x-ray absorption spectroscopy in NiO, *Phys. Rev. B* 51, 13966 (1995).
- ⁵⁷ T. Mizokawa, A. Fujimori, T. Arima, Y. Tokura, N. Mori and J. Akimitsu, Electronic structure of PrNiO_3 studied by photoemission and x-ray-absorption spectroscopy: Band gap and orbital ordering, *Phys. Rev. B* 52, 13865 (1995).
- ⁵⁸ C. Piamonteze, F. M. F. de Groot, H. C. N. Tolentino, A. Y. Ramos, N. E. Massa, J. A. Alonso, and M. J. Martinez-Lope, Spin-orbit-induced mixed-spin ground state in RNiO_3 perovskites probed by x-ray absorption spectroscopy: Insight into the metal-to-insulator transition *Phys. Rev. B* 71, 020406 (2005).
- ⁵⁹ D. Meyers, S. Middey, M. Kareev, M. van Veenendaal, E. J. Moon, B. A. Gray, Jian Liu, J. W. Freeland, and J. Chakhalian, Strain-modulated Mott transition in EuNiO_3 ultrathin films *Phys. Rev. B* 88, 075116 (2013).
- ⁶⁰ R. J. Green, M. W. Haverkort, and G. A. Sawatzky, Bond disproportionation and dynamical charge fluctuations in the perovskite rare-earth nickelates, *Phys. Rev. B* 94, 195127 (2016).
- ⁶¹ A. R. Shelke, C. N. Kuo, S. K. Pandey, T. L. Nguyen, Y. X. Chen, Y. T. Cheng, F. H. Chang, M. Yoshimura, N. Hiraoka, T. W. Pi, and others, Electron spectroscopy study of single crystal CrTe, *Phys. Rev. B* 111, 085142 (2025).
- ⁶² I. I. Mazin, D. I. Khomskii, R. Lengsdorf, J. A. Alonso, W. G. Marshall, R. M. Ibberson, A. Podlesnyak, M. J. Martinez-Lope, and M. M. Abd-Elmeguid, *Phys. Rev. Lett.* 98, 176406 (2007).
- ⁶³ H. Park, A. J. Millis, and C. A. Marianetti, *Phys. Rev. Lett.* 109, 156402 (2012).
- ⁶⁴ S. Johnston, A. Mukherjee, I. Elfimov, M. Berciu, and G. A. Sawatzky, Charge Disproportionation without Charge Transfer in the Rare-Earth-Element Nickelates as a Possible Mechanism for the Metal-Insulator Transition, *Phys. Rev. Lett.* 112, 106404 (2014).
- ⁶⁵ A. Subedi, O. E. Peil, and A. Georges, *Phys. Rev. B* 91, 075128 (2015).
- ⁶⁶ P. Seth, O. E. Peil, L. Pourovskii, M. Betzinger, C. Friedrich, O. Parcollet, S. Biermann, F. Aryasetiawan, and A. Georges, Renormalization of effective interactions in a negative charge transfer insulator, *Phys. Rev. B* 96, 205139 (2017).
- ⁶⁷ D. K. G. deBoer, C. Haas, and G. A. Sawatzky, Auger spectra of compounds of Sc, Ti and Cr, *J. Phys. F: Met. Phys.* 14, 2769 (1984).
- ⁶⁸ C. W. Chuang, Y. Tanaka, M. Oura, K. Rossnagel and A. Chainani, Attractive Coulomb interaction, temperature-dependent hybridization, and natural circular dichroism in $1T\text{-TiSe}_2$, *Phys. Rev. B* 102, 195102 (2020).
- ⁶⁹ J. Zaanen and G. A. Sawatzky, Systematics in Band Gaps and Optical Spectra of 3D Transition Metal Compounds, *Jl. Solid State Chem.* 88, 8 (1990).
- ⁷⁰ A. E. Bocquet, T. Saitoh, T. Mizokawa and A. Fujimori, Systematics in the electronic structure of 3d transition metal compounds, *Solid State Communications* 83, 11 (1992).
- ⁷¹ A. Fujimori, A. E. Bocquet, T. Saitoh and T. Mizokawa, Electronic structure of 3d transition metal compounds: systematic chemical trends and multiplet effects, *Solid State Communications* 83, 11 (1992).
- ⁷² A. Fujimori, *Ligand Field and Charge Transfer in Transition metal compounds*, *Jl. Phys. Soc. Jpn.* 93, 121002 (2024).

Supplementary Information contains following Supplementary Notes:

SN1: Methods

1. Synthesis and structure characterization
2. Electron spectroscopy
3. Cluster-model calculations

SN2: Core level analysis of CoTe₂

SN3: Off-resonant valence band spectra of CoTe₂

SN4: Optimization of electronic parameters in cluster model calculations

1. The 2*p* PES and *L*-edge XAS spectra of CoTe₂
2. The 2*p* PES and *L*-edge XAS spectra of CoO

SN5: Comparison of CoTe₂ and RNiO₃ electronic structure

SN6: Characterizing the effective negative- $\Delta(\leq\Delta_C)$ and effective positive- $\Delta(>\Delta_C)$ regions

A. SN1:Methods

1. 1. Synthesis and structure characterization

The single crystals of CoTe₂ were prepared by the chemical vapor transport method, using iodine as the transport agent^{R1}. High-purity Co (99.95%) and Te (99.999%) powders were mixed with a small amount of iodine (40 mg), sealed in an evacuated quartz tube, and then heated for 15 days in a two-zone furnace with a source zone temperature of 825°C and a growth zone temperature of 750°C. Finally, the quartz tube was quenched into an ice-water bath from the growth temperature of 825°C. The obtained single crystals are hexagonal in shape with typical dimensions of 2 mm×2 mm×0.1 mm. A similar protocol with slightly different temperatures and heating time were used for 1T-NiTe₂ as reported earlier^{R2}. The crystal structure was characterized using powder X-ray diffraction (XRD) (Bruker D2 phaser diffractometer) with Cu-K α radiation. The single crystal quality was confirmed and crystallization directions were identified by the Laue diffraction method (Photonic Science). The XRD results showed a 1T-CdI₂-type trigonal structure (space group of P $\bar{3}$ m1 (No. 164)) with the flat-plates corresponding to the (001) plane. The obtained lattice parameters of CoTe₂ are $a = b = 3.791\text{\AA}$ and $c = 5.417\text{\AA}$ ($c/a = 1.429$), and for NiTe₂ are $a = b = 3.853\text{\AA}$ and $c = 5.260\text{\AA}$ ($c/a = 1.365$). These values are very close to reported values of $a = b = 3.804\text{\AA}$ and $c = 5.417\text{\AA}$ ($c/a = 1.424$) for CoTe₂ and $a = b = 3.843\text{\AA}$ and $c = 5.266\text{\AA}$ ($c/a = 1.370$)^{R3}. It is known that CoTe₂/NiTe₂ exhibit a stable divalent state of Co²⁺/Ni²⁺ ions and the Te atoms are dimerized (Te₂²⁻)^{R4,R5}. It was shown that the Te-Te distance along the *c*-axis (3.446Å and 3.521Å for CoTe₂; 3.429Å and 3.461Å for NiTe₂) were much smaller than the sum of two Te²⁻ ionic radii [$r(\text{Te}^{2-}) = 2.21\text{\AA}$; ref.^{R6}] due to dimerization. The reduced Te-Te distance along the *c*-axis results in a significantly reduced c/a (~ 1.27 - 1.43) for many late TM ditellurides compared to early TM ditellurides such as TiTe₂, ZrTe₂ and HfTe₂ which show a much larger c/a (~ 1.68 - 1.73)^{R4}.

2. 2. Electron spectroscopy

Hard x-ray photoemission spectroscopy (HAXPES) core level and valence band measurements were carried out at BL-12XU (Taiwan Beamline), SPring8, Japan using linearly polarized X-ray beam with incident photon energy $h\nu = 6.5$ keV. Liquid He closed cycle cryostat was used to cool the sample, down to a temperature of $T = 25$ K. The Fermi level E_F of a Au thin film was also measured at $T = 25$ K to calibrate the binding energy(BE) scale. The total energy resolution is 270 meV as estimated from the fitting of Au E_F . The single crystal samples were cleaved using a top-post in ultra-high vacuum (UHV) of 5.5×10^{-9} mbar in the preparation chamber and then quickly transferred to the main chamber at 7.0×10^{-10} mbar for the measurements. Soft x-ray PES (SX PES) core level and valence band, XAS and 2*p*-3*d* resonant-PES measurements were carried out at BL-17SU RIKEN beamline in SPring-8, Japan using a circularly polarized x-ray beam. The metal $L_{3,2}$ -edge and Te $M_{5,4}$ -edge XAS measurements were carried out in total electron yield mode. SX PES core levels and valence band measurements were carried out with incident photon energy $h\nu = 1.5$ keV, except for the Co 2*p* and Te 3*p* core levels which were measured with $h\nu = 1.7$ keV to avoid overlapping Auger lines in the spectrum at $h\nu = 1.5$ keV. A Liquid N₂ flow-type cryostat was used to cool the sample down to 80 K. The total energy resolution at $T = 80$ K is 400 meV with $h\nu = 1.5$ keV, as obtained from a fit to the Au E_F . The samples were cleaved and measured in the main chamber at a UHV of 1.0×10^{-10} mbar. The resonant PES spectra, obtained using $h\nu = 770 - 803$ eV, were normalized to the peak intensity of shallow 4*d* core-level peaks (bright vertical lines at ~ 41 and 42 eV BEs, in Fig. 1(a) map of the main paper).

3. 3. Cluster-model calculations

The metal 2*p* PES core level and $L_{3,2}$ -edge XAS spectra were calculated based on a charge transfer multiplet cluster model using the QUANTY code^{R7-R9}. The divalent ions of Co²⁺ and Ni²⁺ correspond to $3d^7$ and $3d^8$ electronic configurations, respectively. A ML_6 cluster with octahedral symmetry (O_h), $M = \text{Co/Ni}$ atoms and L is ligand Te atoms. The initial state consists of a linear combination of $|3d^n\rangle$, $|3d^{n+1}\underline{L}^1\rangle$ and $|3d^{n+2}\underline{L}^2\rangle$ states, where \underline{L} corresponds to hole in ligand states. The electronic parameters of the calculation are; the on-site Coulomb energy U_{dd} (obtained from the Cini-Sawatzky analysis), the charge transfer energy Δ is the energy difference between $|3d^n\rangle$ and $|3d^{n+1}\underline{L}^1\rangle$ states, the 3*d*-Te 5*p* hybridization strength (T_{eg} and $T_{t2g} = T_{eg}/2$) and the crystal field splitting $10Dq$ between t_{2g} and e_g orbitals. For calculating the 2*p* PES spectrum, the final state is a free electron with a core hole in the 2*p* level and includes the on-site core hole potential U_{pd} on the metal site. The final states for XAS correspond to 2*p*-3*d* dipolar excitations from the metal L edge to the unoccupied d states, and also includes U_{pd} . In principle, one needs to use a series of excited configurations of the d^n state also, but is computationally difficult. In general, it has been found that reducing the the Slater integrals to 80% of their origi-

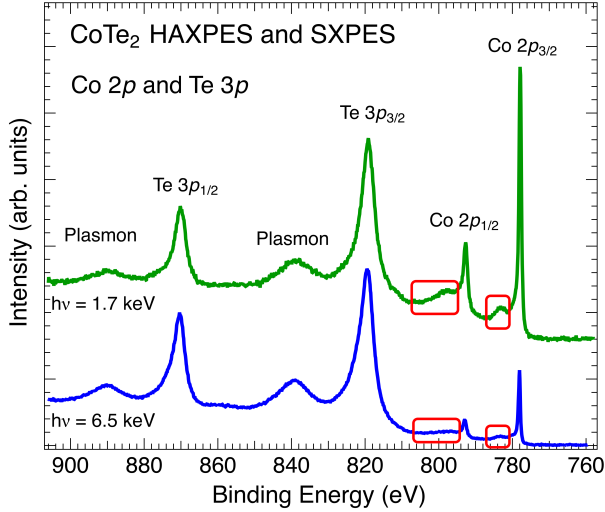


FIG. S1. Co $2p$ and Te $3p$ core level spectra of CoTe_2 single crystal measured at $T = 20$ K with $h\nu = 6.5$ keV (HAXPES) and at $T = 80$ K with $h\nu = 1.7$ keV (SXPES)

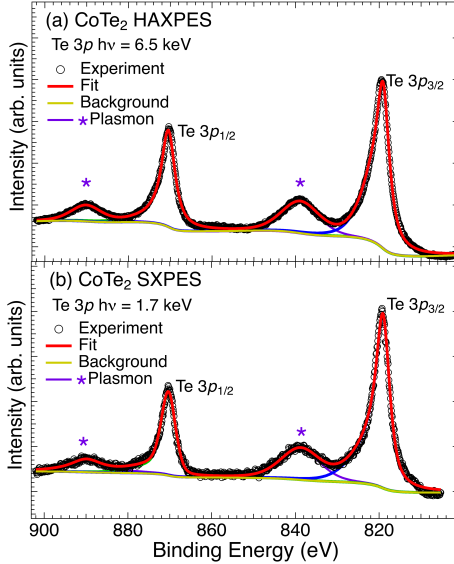


FIG. S2. Least square fitting of Te $3p$ core levels of CoTe_2 single crystal measured using (a) HAXPES and (b) SXPES techniques

nal Hartree-Fock values, the deviation of calculations compared to experimental results can be minimized by applying this semi-empirical correction to the Slater integrals^{R10}. The calculated spectrum is obtained by convoluting the discrete final states by broadening it with a Lorentzian function for $2p_{3/2}$ and $2p_{1/2}$ lifetimes, respectively) and a Gaussian function for the experimental spectral width.

TABLE I. Fitting parameters of Te $3p$ core levels of CoTe_2 single crystal measured using HAXPES and SXPES

Fit component	Binding Energy (eV)	FWHM (eV)
HAXPES		
Te $3p_{3/2}$	819.06	3.72
Te $3p_{1/2}$	870.16	3.89
Plasmon	838.86	10.50
Plasmon	890.15	8.33
SXPES		
Te $3p_{3/2}$	819.12	3.83
Te $3p_{1/2}$	870.24	3.97
Plasmon	838.79	11.04
Plasmon	889.96	9.50

TABLE II. Fitting parameters of Te $3d$ core level of CoTe_2 using HAXPES and SXPES

Fit component	Binding Energy (eV)	FWHM (eV)
HAXPES		
Te $3d_{5/2}$	572.53	0.76
Te $3d_{3/2}$	582.94	0.80
Plasmon	592.20	6.50
Plasmon	602.57	6.00
SXPES		
Te $3d_{5/2}$	572.50	1.03
Te $3d_{3/2}$	582.89	1.06
Plasmon	592.15	8.01
Plasmon	602.52	5.90

B. SN2: Core level analysis of CoTe_2

Figure S1 shows a wide spectral range covering the Co $2p$ and Te $3p$ core levels, measured with HAXPES ($h\nu = 6.5$ keV) and SXPES ($h\nu = 1.7$ keV). Based on the binding energy (BE) positions of the high intensity peaks, the four main peaks of Co $2p_{3/2}$, Co $2p_{1/2}$, Te $3p_{3/2}$ and Te $3p_{1/2}$ can be suitably assigned^{R11}. Since the Co $2p$ and Te $3p$ core levels have significantly different photoionization cross section (PICS)^{R12} with $h\nu = 6.5$ keV and $h\nu = 1.7$ keV, the data are normalized at the Te $3p_{1/2}$ main peak to see the relative change in Co $2p$ core levels at different photon energies. As is clear from Fig. S1, the SXPES Co $2p$ spectra show a much higher intensity of the main peaks compared to the HAXPES data. In addition to the main peaks, low intensity satellites are observed at higher BEs to the four main peaks. While the low intensity satellites at higher BEs of the Te $3p_{3/2}$ and Te $3p_{1/2}$ look very similar in shape and widths for both HAXPES and SXPES data, the low intensity satellites of Co $2p_{3/2}$ and Co $2p_{1/2}$ seem to show differences in HAXPES and SXPES data. In particular, the satellite of the Co $2p_{1/2}$ peak seems to show higher intensity than the satellite of the Co $2p_{3/2}$ peak, and opposite to the behavior of the Te $3p_{1/2}$ satellite which shows slightly lower intensity compared to the Te $3p_{3/2}$ satellite. Further, the Co $2p_{3/2}$ and Co $2p_{1/2}$ satellites in the HAXPES data seem to show very small intensity compared to the SXPES data.

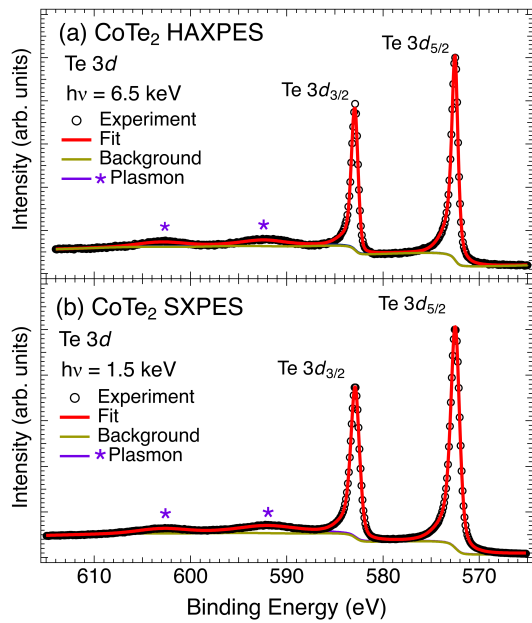


FIG. S3. Least square fitting of Te $3d$ core level CoTe₂ single crystal measured using (a) HAXPES and (b) SXPES techniques

In order to quantify the peak energy positions and shapes, and to clarify the character and difference between the Co $2p_{3/2}$ and $2p_{1/2}$ main peaks and satellites, as well as for Te $3p_{3/2}$ and $3p_{1/2}$ main peaks and satellites, we first carried out a least-squares fitting of the simpler case of Te $3p_{3/2}$ and Te $3p_{1/2}$ HAXPES and SXPES core levels. The main peaks could be fitted with single asymmetric Voigt functions typical of metals, while the satellites required a symmetric Gaussian function. The results are shown in Fig. S2(a) and S2(b) with the fits (full lines) overlaid on the experimental spectra (empty circles). The peak energy positions and peak full-widths and half maximum (FWHM) are listed in Table I. The main peak BEs are very similar: 819.06 eV and 870.16 eV in HAXPES and 819.12 eV and 870.24 eV in SXPES, and the separation in both cases ($= 51.1 \pm 0.1$ eV) is quite close to the known Te $3p_{3/2}$ and Te $3p_{1/2}$ spin-orbit splitting of 51.0 eV^{R11}. The observed BE values are slightly lower compared to the elemental Te $3p_{3/2}$ and Te $3p_{1/2}$ values.^{R11} The broad satellites in HAXPES and SXPES data are positioned at 19.8 ± 0.2 eV higher BE to Te $3p_{3/2}$ and Te $3p_{1/2}$ main peaks, and suggest a plasmon origin of the satellites.

For verifying the plasmon origin of the satellites, we measured another pair of core-levels, namely, the Te $3d$ core levels, using HAXPES and SXPES as shown in Fig. S3(a) and S3(b). A least-squares fitting to the Te $3d_{5/2}$ and Te $3d_{3/2}$ main peaks and weak satellites is superimposed as full lines on the experimental spectra (empty circles). Here again, the main peaks were fitted with single asymmetric Voigt functions, and the satellites with symmetric Gaussian functions. The peak energy positions and peak FWHMs are listed in Table II. The sharp intense lines at 572.53 eV and 582.94 eV in HAXPES and 572.50 eV and 582.89 eV in SXPES are the Te $3d_{5/2}$ and Te $3d_{3/2}$ main peaks, respectively. Their observed

TABLE III. Fitting parameters of Co $2p$ core levels of CoTe₂ single crystal measured using HAXPES and SXPES

Fit component	Binding Energy (eV)	FWHM (eV)
HAXPES		
Co $2p_{3/2}$	778.06	0.63
Co $2p_{1/2}$	792.86	0.95
Co $2p_{3/2}$ Satellite	783.01	3.33
Co $2p_{1/2}$ Satellite	795.47	3.21
Co $2p_{3/2}$ Plasmon	797.82	4.31
SXPES		
Co $2p_{3/2}$	777.90	0.70
Co $2p_{1/2}$	792.70	1.14
Co $2p_{3/2}$ Satellite	783	3.36
Co $2p_{1/2}$ Satellite	795.65	3.30
Co $2p_{3/2}$ Plasmon	797.76	4.44

BEs are very consistent with earlier reports of measured Te $3d$ core levels of CoTe₂^{R13,R14}. The Te $3p$ and Te $3d$ core levels of NiTe₂^{R15} are also very similar to those of CoTe₂. The measurements reported by Hu et al.^{R14} was on CoTe₂ samples from the same batch as present work, while the aim of that study was to check the feasibility of making terahertz nonlinear Hall rectifiers using mechanically exfoliated CoTe₂. The narrow single main peaks of $3d_{5/2}$ and Te $3d_{3/2}$ and the absence of any feature ≈ 3.0 eV above the main peaks indicates absence of oxidation in the HAXPES and SXPES spectra^{R14}. Most importantly, the broader low intensity features are positioned at 19.65 ± 0.1 eV higher BEs and confirm the plasmon origin, consistent with Te $3p$ HAXPES and SXPES core levels. This hints at the possibility of a plasmon feature of the Co $2p_{3/2}$ main peak overlapping the satellite feature of the Co $2p_{1/2}$ main peak.

In order to check the above possibility, we then carried out a least square fit of the Co $2p$ core levels of HAXPES and SXPES shown in Fig. S4(a) and S4(b), respectively. The fitting results showing the peak energy positions and peak FWHMs are listed in Table III. The Co $2p_{3/2}$ and Co $2p_{1/2}$ main peaks could be fitted with asymmetric Voigt line shapes, consistent with the metallic nature of CoTe₂. Their observed BEs are 778.06 eV and 792.86 eV, respectively for HAXPES, and 777.90 eV and 792.70 eV, respectively for SXPES. These values are also consistent with previously measured Co $2p$ core levels of CoTe₂^{R13,R14}. While the Co $2p_{3/2}$ range could be fitted by a single main peak and a single weak satellite feature, the Co $2p_{1/2}$ spectral range required a single main peak and two weak features. From the values of the peak energy positions (Table III), it is clear that the second weak feature lies at a BE of 19.8 ± 0.1 eV above the Co $2p_{3/2}$ main peak, consistent with the plasmons lying at a BE of 19.8 ± 0.2 eV/ 19.65 ± 0.1 eV above the Te $3p$ and $3d$ spectra, respectively. This confirms that the second weak feature corresponds to a plasmon feature of the Co $2p_{3/2}$ main peak, lying very close to the Co $2p_{1/2}$ satellite. It was important to identify and separate out the plasmon feature from the Co $2p_{1/2}$ satellite, as it then allowed us to carry out a cluster model calculation of the intrinsic main peak and satellites of the Co $2p$ spectrum shown in Fig. 3(a)

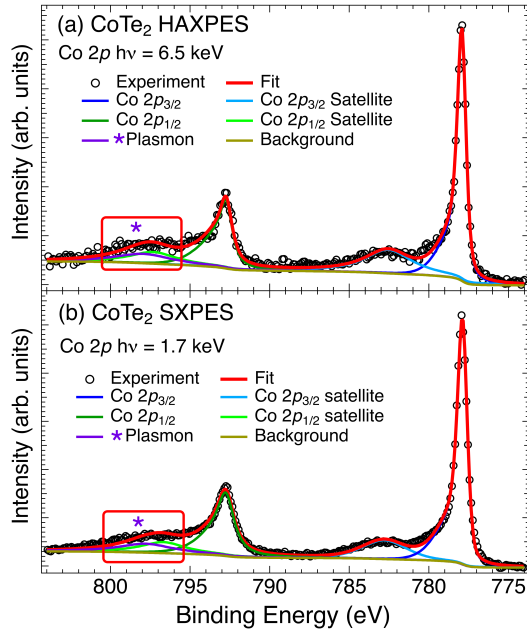


FIG. S4. Least square fitting of Co $2p$ core levels of CoTe_2 single crystal measured using (a) HAXPES and (b) SXPES techniques to separate out the plasmon of Co $2p_{3/2}$ core level lying at a BE close to the Co $2p_{1/2}$ core level satellite.

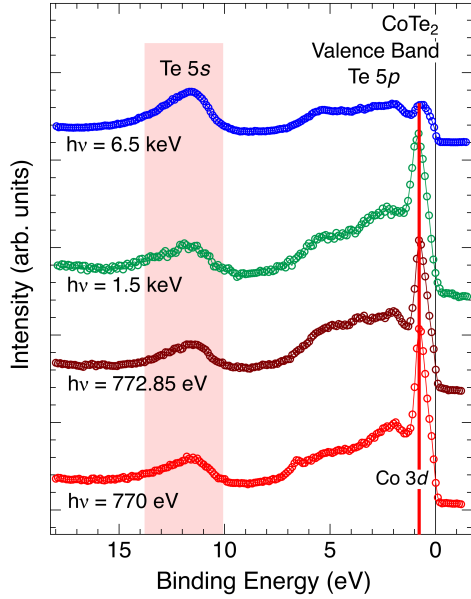


FIG. S5. CoTe_2 valence bands measured at different photon energies, namely $h\nu = 772$ eV, $h\nu = 775$ eV, $h\nu = 1.5$ keV and $h\nu = 6.5$ keV

of the main paper.

C. SN3: Off-resonant valence band spectra of CoTe_2

With the aim of separating out the Te $5p$ partial density of states (PDOS) from the Co $3d$ PDOS based on their pho-

toionization cross-sections (PICS)^{R12}, we plot in Fig. S5 the valence band spectra over a large BE energy range using off-resonant photon energies $h\nu = 770$ eV, 772.85 eV, 1.5 keV and 6.5 keV. The Fig. S5 spectra are normalized at the Te $5s$ shallow core level at ≈ 12 eV BE so as to emphasize the relative spectral weights of Te $5p$ states and Co $3d$ states. Fig. S5 shows that the weight of Co $3d$ PDOS peak at 0.8 eV BE does not change much for $h\nu = 770$ eV, 772.85 eV, and 1.5 keV but gets strongly suppressed for $h\nu = 6.5$ keV. This is due to the strongly reduced PICS of Co $3d$ PICS compared to Te $5p$ PICS at $h\nu = 6.5$ keV. The Te $5p$ states are spread from E_F (as will be clarified below) to about 7 eV BE and show small variation in intensity due the change in PICS with $h\nu = 770$ eV, 772.85 eV, 1.5 keV. But at $h\nu = 6.5$ keV, the Te $5p$ states dominate the spectrum as the PICS^{R12} ratio of Te $5p$:Co $3d$ is 9.47 . Most importantly, the small peak near E_F measured with $h\nu = 6.5$ keV shows a different shape and width compared to the Co $3d$ peak with lower $h\nu$ values and this is discussed in more detail in Fig. 2(a) of the main paper, together with off- and on-resonant Co $2p - 3d$ resonant-PES spectra.

D. SN4: Optimization of electronic parameters in cluster model calculations

Charge-transfer cluster model spectral calculations as described in the Methods section were carried out to obtain optimal electronic parameters which can suitably describe the $2p$ PES and L -edge XAS experimental spectra of CoTe_2 and CoO , as discussed in the main paper (Fig. 3a-d). The full set of optimal parameters are listed in Table IV for CoTe_2 and CoO . It is clear that the electronic parameters of CoTe_2 and CoO are quite different with a negative and positive Δ , respectively. In order to validate the obtained electronic parameters, we carried out a systematic and extensive set of calculations to confirm their optimal values and we discuss a few of them in the following. It is noted that the present study is the first to report a comparison of the $2p$ PES and L -edge XAS experimental and calculated spectra to obtain electronic parameters of CoTe_2 . On the other hand, CoO has been analyzed earlier^{R16,R17} and the parameters for CoO that we obtained are quite close to an analysis using a cluster model^{R16} as well as a charge-transfer multiplet calculation combined with DMFT method^{R17}, as shown in Table IV.

1. Simultaneous optimization of the $2p$ PES and L -edge XAS spectra of CoTe_2

In Fig. S6(a) and (b), we plot a series of Co $2p$ PES and L -edge XAS calculated spectra (blue lines) for CoTe_2 , respectively, and compare it with experiment (red symbols) for checking the optimal value of the charge transfer energy Δ . We varied $\Delta = -3.0$ to $+2.0$ eV in 1 eV steps, keeping all other parameters fixed to optimal values. In particular, the results show that the Co $2p_{3/2}$ PES and L -edge XAS satellite feature in the calculated spectra show the least deviation compared to experiment for $\Delta = -2.0$ eV.

TABLE IV. Electronic parameters and d^n count for CoTe₂ and CoO using 3-basis state cluster model calculations.

	CoTe ₂	CoO	CoO ref. ^{R16}	CoO ref. ^{R17}
Parameter				
U_{dd} (eV)	3.0	5.0	5.3	6.8
Δ (eV)	-2.0	4.0	5.5	4.1
T_{eg} (eV)	1.2	2.5	2.25	2.0
T_{t2g} (eV)	0.6	1.25	1.0	1.2
$10Dq$ (eV)	1.0	0.5	0.7	0.25
F_k, G_k	0.5	0.8	0.8	0.8
U_{dd}/T_{eg}	2.5	2.0	2.3	3.4
$ \Delta /T_{eg}$	1.7	1.6	2.4	2.05
d^n count	8.14	7.21	7.22	–

Similarly, Fig. S6(c) and (d) shows a series of Co 2p PES calculated spectra (blue lines) for CoTe₂ for checking the optimal value of the Slater parameters F_k and G_k independently i.e. by varying only one of them at a time by a reduction factor of 0.8, which is the standard reduction value as discussed in the Methods section. However, it was found that changing only of them, either F_k or G_k , did not give a suitable match to experimental data. In particular, the Co 2p_{3/2} satellite feature showed significant deviations from experimental spectra (red symbols). It was found that we need to change both of them simultaneously to minimize the deviation of the Co 2p_{3/2} satellite feature compared to experiment. The results of such an exercise is shown in Fig. S6(e) and (f), where we plot a series of Co 2p PES and *L*-edge XAS calculated spectra (blue lines) for CoTe₂, respectively, compared with experiment (red symbols). We varied F_k and G_k together from a reduction factor of 0.8 to 0.1, keeping all other parameters fixed to optimal values. The results show that a reduction factor of 0.5 for F_k and G_k shows the least deviation compared to experiment for the Co 2p PES and *L*-edge XAS spectra.

2. Simultaneous optimization of the 2p PES and *L*-edge XAS spectra of CoO

Fig. S7(a) and (b) shows a series of Co 2p PES and *L*-edge XAS calculated spectra (blue lines) for CoO, respectively, for checking the optimal value of the on-site Coulomb energy U_{dd} and compare it with experiment (green symbols). We varied $U_{dd} = 4.0$ to 7.0 eV in 1 eV steps, keeping all other parameters fixed to optimal values. The experimental Co 2p HAXPES spectrum is taken from ref.^{R18}. The results show that, compared to the optimal value of $U_{dd} = 5.0$ eV, the Co 2p_{3/2} satellite feature in the calculated spectra deviates from experiment for larger U_{dd} values. On the other hand, both, the Co 2p_{3/2} and Co 2p_{1/2} satellite features in the calculated spectra together deviate from experiment for smaller U_{dd} values compared to the spectrum obtained with the optimal value of $U_{dd} = 5.0$ eV.

Fig. S7(c) and (d) shows Co 2p PES and *L*-edge XAS calculated spectra (blue lines) for CoO, respectively, for checking

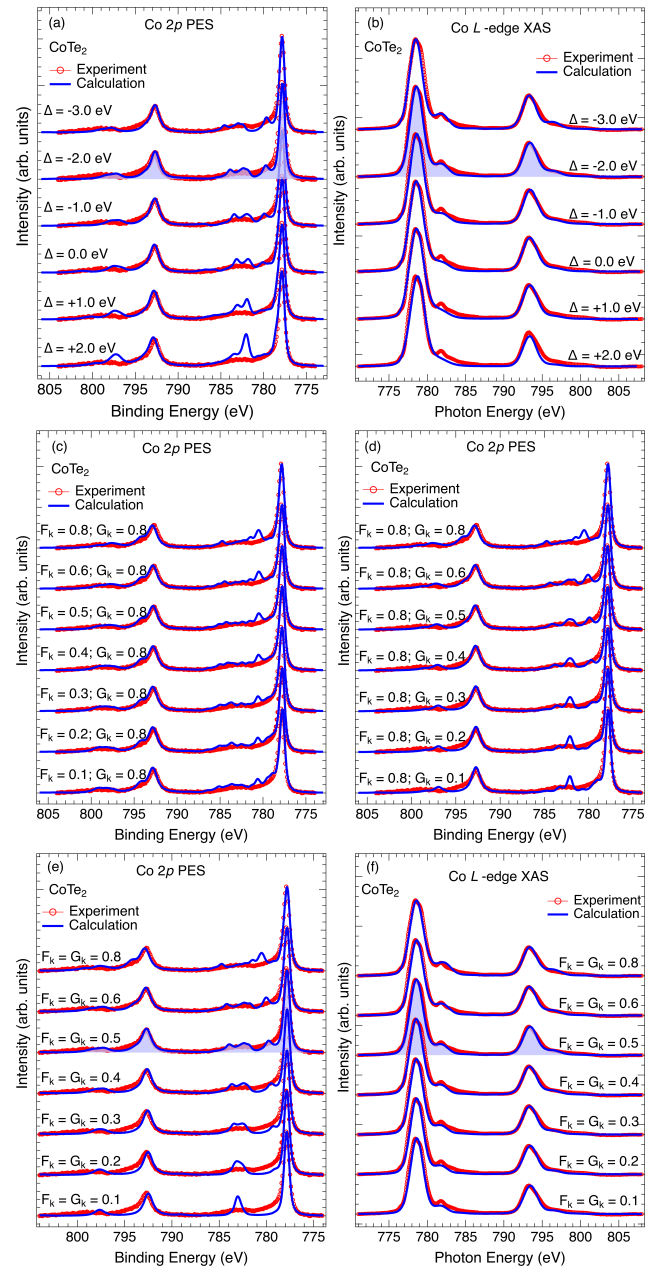


FIG. S6. (a,b) Simultaneous optimization of charge-transfer energy Δ for (a) Co 2p PES and (b) Co *L*-edge XAS of CoTe₂. (c) Attempt at optimization of F_k from 0.8 to 0.1 by keeping $G_k = 0.8$ for Co 2p PES. (d) Attempt at optimization of G_k from 0.8 to 0.1 by keeping $F_k = 0.8$ for Co 2p PES. (e,f) Simultaneous optimization of F_k and G_k from 0.8 to 0.1 for (e) Co 2p PES and (f) Co *L*-edge XAS.

the optimal value of the the charge transfer energy Δ and compare it with experiment (green symbols). We varied $\Delta = 1.0$ to $+6.0$ eV in 1 eV steps, keeping all other parameters fixed to optimal values. It is observed in Fig. S9(a) that the Co 2p_{3/2} satellite feature in the calculated spectra shows least deviation for $\Delta = 4.0$ eV. But shows deviations from experimental main peak widths and satellite widths and intensities for $\Delta < 4.0$ eV, and to a lesser extent also for $\Delta > 4.0$ eV. A similar behavior

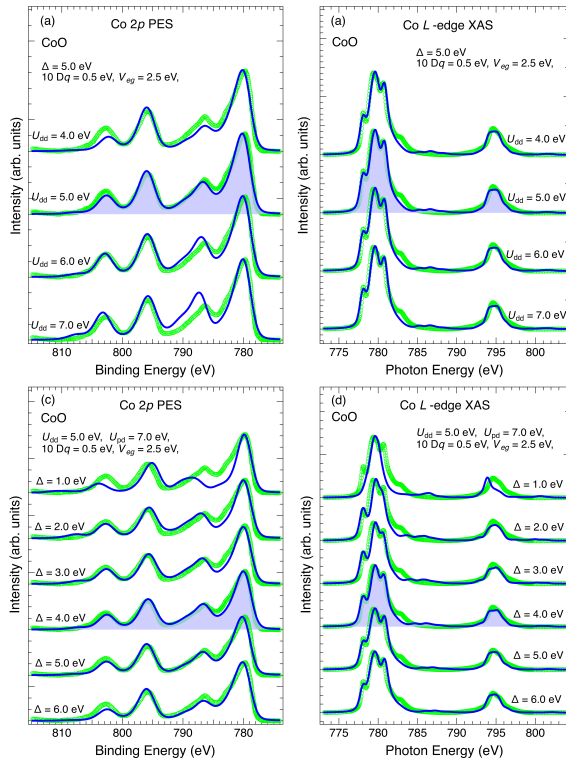


FIG. S7. (a,b) Simultaneous optimization of on-site energy U_{dd} for Co 2p PES and Co L -edge XAS of CoO. (c,d) Simultaneous optimization of charge-transfer energy Δ for (c) Co 2p PES and (d) Co L -edge XAS of CoO.

for $\Delta < 4.0$ eV is also seen in the Co L -edge XAS spectra for CoO shown in Fig. S9(b). However, the Co L -edge XAS spectrum for $\Delta = 4.0$ eV shows the least deviation in the leading edge prepeak/multiplet compared to also the spectra obtained for $\Delta > 4.0$ eV. Taken together, the simultaneous optimization of Co 2p PES and L -edge XAS spectra with $\Delta = 4.0$ eV is considered to show least deviation compared to experiment.

E. SN5: Comparison of CoTe₂ and RNiO₃ electronic structure parameters

It is important to discuss and compare the electronic structure of RNiO₃ materials in the high temperature metallic phase with CoTe₂, as the formally Ni³⁺ ions in RNiO₃ have the same $3d^7$ electron configuration like Co²⁺ in CoTe₂. As briefly mentioned in the main paper, early single metal-site cluster model calculations^{R19–R21} for the XAS of the metallic RNiO₃ phase used a small positive- Δ while the most recent study^{R22} used a negative- Δ , but all of them concluded a dominantly charge transferred ground state (with weights of $d^{n+1}\underline{L}^1 + d^{n+2}\underline{L}^2 > d^n$). In Table V, we compare the electronic parameters, the spin magnetic moment m_S , weights in the ground state and total d^n counts for CoTe₂ with two cases of RNiO₃ reported in the literature^{R19, R22}. It shows a dominantly $d^{n+1}\underline{L}^1$ ground state character using single metal-

TABLE V. Electronic parameters, spin magnetic moments m_S , weights in the ground state and total d^n -counts for CoTe₂ and RNiO₃ (metal phase) using single metal-site cluster model calculations.

	CoTe ₂	RNiO ₃ ref. ^{R57}	RNiO ₃ ref. ^{R60}
Parameter			
U_{dd} (eV)	3.0	7.0	6.0
Δ (eV)	-2.0	1.0	-0.5
T_{eg} (eV)	1.2	2.6	3.0
T_{t2g} (eV)	0.6	1.2	1.74
$10Dq$ (eV)	1.0	0.6	0.95
m_S (μ_B)	0.9	0.9	1.1
d^7 weight	11.0%	34%	24%
$d^8\underline{L}^1$ weight	64%	56%	61%
$d^9\underline{L}^2$ weight	25%	10%	15%
d^n count	8.14	7.76	7.83

site cluster model calculations RNiO₃, as is also obtained for CoTe₂ in the present study.

Further, several theoretical calculations^{R23–R27} have been carried out to address the CDW transition mechanism and role of Coulomb correlations. In spite of the different theoretical methods, all of them agree that the Ni³⁺ $3d^7$ state gets stabilized to a dominantly $3d^8\underline{L}^1$ ground state in the high- T metallic phase, consistent with a negative- Δ . Based on a low-energy description involving e_g -orbitals and LDA+ U calculations ($U = 5$ eV; Hund's coupling $J_H = 1$ eV), Mazin et al.^{R23} clarified that a CDW of the type $2e_g^1 \rightarrow e_g^0 + e_g^2$ is favored if e_g bandwidth becomes larger than the Jahn-Teller splitting and J_H reduces U to U_{eff} . Park et al.^{R24} carried out DFT+DMFT calculations (also with $U = 5$ eV; $J_H = 1$ eV) and showed that neighboring Ni sites show long Ni₁-O bonds ($3d^8$ with $S=1$; paramagnetic Curie-type local susceptibility, $\chi(T) \sim 1/T$) and short Ni₂-O bonds ($3d^8\underline{L}^2$ with $S=0$; paramagnetic metal type T -independent χ) and called it a "site-selective Mott transition". Johnston et al.^{R25} reported exact diagonalization calculations of Ni₂O₁₀ clusters as well as Hartree-Fock calculations, and obtained a metal to a CDW gapped state with two types of Ni ions, upon increasing distortion. Subedi et al.^{R26} calculated a phase diagram using DFT+DMFT calculations and showed that if $U_{eff} = U - 3J_H \lesssim 0$, where U and J_H are not the atomic values but the renormalized values for hybridized e_g states, it causes a spontaneous bond disproportionation for large enough J_H . Seth et al.^{R27} used a GW+DMFT scheme^{R28} to show that U and J_H indeed get reduced, and a CDW phase is stabilized on including an intersite Coulomb interaction. These studies concluded that a small or negative U_{eff} is qualitatively consistent with a negative- Δ . However, our results for determining U_{dd} using the Cini-Sawatzky analyses indicate moderate values of $U_{dd} = 3.0$ and 3.7 eV for CoTe₂ (main paper) and NiTe₂ (ref.^{R15}), respectively. Nonetheless, using these values of U_{dd} , our cluster model calculations indicate CoTe₂ (main paper) and NiTe₂ (ref.^{R15}) are negative- Δ materials with a dominant $3d^{n+1}\underline{L}^1$ contribution in the ground state, indicating a very similar electronic structure like the high temperature metallic phase of RNiO₃.

F. SN6: Characterizing the properties of the effective negative $\Delta \leq \Delta_C$ and effective positive $\Delta > \Delta_C$ regions

In this note, we clarify several aspects of the properties of the effective negative and positive charge-transfer energy Δ regions (labelled A-C in Fig. 4(a) and (b) of the main paper) across the critical Δ_C in CoTe₂ and NiTe₂. Figs. 4(a) and (b) of the main paper show the evolution of the total electron count d^n as a function of T_{eg} for various values of the Δ and U_{dd} , and these energies are defined as multiplet averaged values^{R29-R31}. In the following, we address the role of an effective negative Δ compared to the multiplet averaged Δ and why do we obtain $\Delta_C = 0.25$ eV in Fig. 4(a) and $\Delta_C = -1.55$ eV in Fig. 4(b), when we use other parameters fixed to CoTe₂ and NiTe₂ optimal parameters (main paper; ref.^{R15}), respectively.

In Fig. S8(a), we plot the spin magnetic moment m_S vs. Δ for $T_{eg} = 5$ meV obtained from the same cluster model calculation results shown in Fig. 4(a) of the main paper, using other parameters fixed to CoTe₂ optimal parameters. The m_S values exhibit a jump at $\Delta = 0.25$ eV, where even the total d^n count shows a jump in Fig. 4(a) of the main paper, and we denote it as Δ_C . The m_S values show negligible change for $\Delta \leq \Delta_C$, and also for $\Delta > \Delta_C$. On the other hand, m_S vs. Δ curve for the CoTe₂ optimal value of $T_{eg} = 1.2$ eV, the jump in m_S values gets suppressed and it shows a small gradual increase on increasing Δ . The corresponding individual ground state weights from the cluster model calculations for $T_{eg} = 5$ meV are listed in Table VI. It is clear from Fig. S8(a) and Table VI that for $\Delta \leq \Delta_C$, the results indicate that a dominantly $d^{n+1}\underline{L}^1$ state corresponds to the effective negative- Δ region A of Fig. 4(a), and for $\Delta > \Delta_C$, it indicates a dominantly d^n state and corresponds to the effective positive- Δ region B of Fig. 4(a).

Fig. S8(b) shows the spin magnetic moment m_S vs. Δ for $T_{eg} = 5$ meV obtained from the cluster model calculation results shown in Fig. 4(a) of the main paper, using other parameters fixed to CoO optimal parameters. The m_S values show a negligible change for all Δ values, while the m_S vs. Δ curve for the optimal value of $T_{eg} = 2.5$ eV shows a small gradual increase of m_S on increasing Δ . The results indicate that region C of Fig. 4(a) corresponds to the usual positive- Δ region. It is noted that the m_S values on increasing Δ in Fig. S8(a) connect to the m_S values on increasing Δ in Fig. S8(b), confirming that region B is an effective positive- Δ region. As another check, in Fig. S8(c), we plot the m_S vs. T_{eg} for selected Δ values from regions B and C of Fig. 4(a). The results show jumps corresponding to those seen in the total d^n count in Fig. 4(a), and confirm they are associated with spin-state transitions.

Similarly, in Fig. S8(d), we plot the spin magnetic moment m_S vs. Δ for $T_{eg} = 5$ meV obtained from the cluster model calculation results shown in Fig. 4(b) of the main paper, using other parameters fixed to NiTe₂ optimal parameters. The m_S values exhibit a jump at $\Delta = -1.55$ eV, where even the total d^n count shows a jump in Fig. 4 of the main paper, and we denote it as Δ_C . The m_S values again show a negligible change for $\Delta \leq \Delta_C$, and also for $\Delta > \Delta_C$. Also, for the m_S vs. Δ curve for the optimal value of $T_{eg} = 2.5$ eV, the jump in m_S values gets suppressed and it shows a small gradual increase on increasing Δ . The corresponding individual ground state

TABLE VI. Ground state weights obtained from cluster model calculations with $T_{eg} = 5$ meV, starting with the formal d^7 and d^8 configurations (for CoTe₂ and NiTe₂, respectively).

CoTe ₂	d^7	$d^8\underline{L}^1$	$d^9\underline{L}^2$
$\Delta_C = 0.25$ eV	0.001	0.999	0.000
$\Delta = 0.3$ eV	0.999	0.001	0.000
($> \Delta_C$)			
NiTe ₂	d^8	$d^9\underline{L}^1$	$d^{10}\underline{L}^2$
$\Delta_C = -1.55$ eV	0.103	0.897	0.000
$\Delta = -1.50$ eV	0.958	0.042	0.000
($> \Delta_C$)			

weights from the cluster model calculations with $T_{eg} = 5$ meV are also listed in Table VI. Again, from Fig. S8(d) and Table VI it is clear that for $\Delta \leq \Delta_C$, the results indicate a dominantly $d^{n+1}\underline{L}^1$ state corresponding to the effective negative- Δ region A of Fig. 4(b), and for $\Delta > \Delta_C$, it corresponds to the effective positive- Δ region B of Fig. 4(b).

Fig. S8(e) shows the spin magnetic moment m_S vs. Δ for $T_{eg} = 5$ meV obtained from the cluster model calculation results shown in Fig. 4(b) of the main paper, using other parameters fixed to NiO optimal parameters. The m_S values show a negligible change for all Δ values. On the other hand, m_S vs. Δ curve, plotted for the optimal value of $T_{eg} = 2.4$ eV, shows a small gradual increase of m_S on increasing Δ . The results indicate that region C of Fig. 4(b) corresponds to the positive- Δ region. Also, the m_S values on increasing Δ in Fig. S8(d) connect to the m_S values on increasing Δ in Fig. S8(e), confirming that region B is an effective positive- Δ region. Since the estimated crystal field splitting $10Dq = 0.5$ eV in NiTe₂, it does not show spin state transitions in region B.

Finally, we answer the question about why $\Delta_C = 0.25$ eV in CoTe₂ and $\Delta_C = -1.55$ eV NiTe₂. The Δ as used in the present cluster model calculations is defined as,

$$\Delta = E(d^{n+1}\underline{L}^1) - E(d^n),$$

where $E(d^n)$ is the center of gravity or average energy of the d^n multiplets and $E(d^{n+1}\underline{L}^1)$ is the center of gravity or average energy of $d^{n+1}\underline{L}^1$ multiplets. The charge transfer energy can be also defined by using the energies of the lowest multiplet of $d^{n+1}\underline{L}^1$ and d^n configurations^{R29-R31}. This is relevant because the low energy properties of transition metal compounds are mainly determined by excitations associated with the lowest energy multiplets. If we denote the energy difference between the energy of the lowest multiplet and the average multiplet energy as $\Delta' E_n$, then the effective charge transfer energy Δ_{eff} , is given by

$$\Delta_{eff} = \Delta + \Delta' E_{n+1} - \Delta' E_n.$$

Accordingly, one can check when does the ground state transform from a dominantly d^n state to $d^{n+1}\underline{L}^1$ state i.e. negative Δ represents $\Delta < 0$ or $\Delta_{eff} < 0$? Using the same cluster model calculations discussed above, we calculate L -edge XAS spectra with a small $T_{eg} = 5$ meV for various Δ values at and across Δ_C , with a very small Gaussian broadening of 0.1 eV FWHM as shown in Fig. S9. The L -edge XAS spectrum corresponds to transitions from the ground state to final states

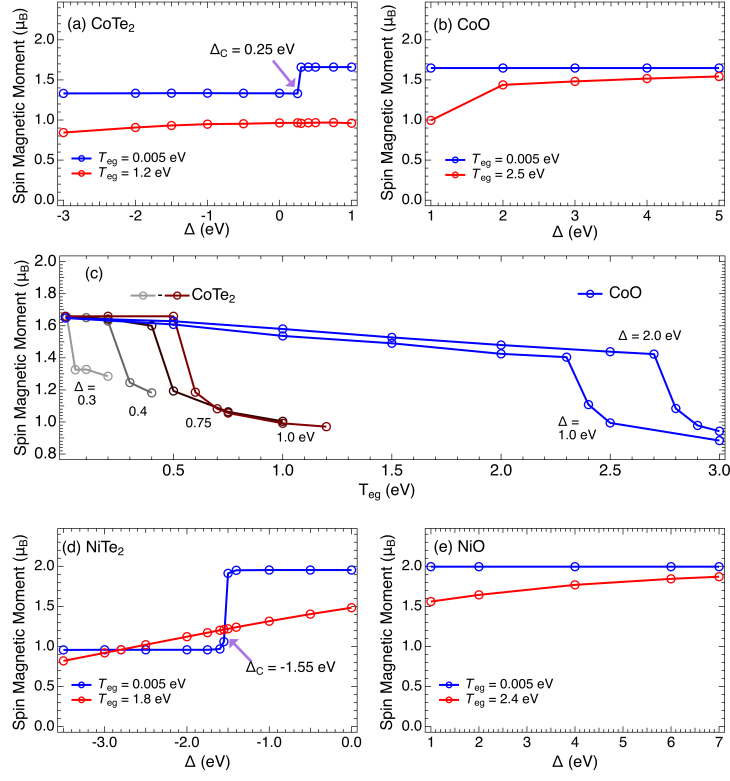


FIG. S8. (a) In CoTe₂, the spin magnetic moment m_S vs. Δ for $T_{eg} = 5$ meV, exhibits a jump at $\Delta_C = 0.25$ eV, while for optimal $T_{eg} = 1.2$ eV, m_S vs. Δ shows a gradual change across Δ_C . (b) In CoO, the m_S vs. Δ shows a nearly constant value for small $T_{eg} = 5$ meV, while for $\Delta \leq 2.0$ eV, a small jump is observed in m_S vs. T_{eg} , for optimal $T_{eg} = 2.5$ eV. (c) The jumps seen in regions B and C are also confirmed to be associated with spin-state transitions. (d) In NiTe₂, the spin magnetic moment m_S vs. Δ for $T_{eg} = 5$ meV, exhibits a jump at $\Delta_C = -1.55$ eV, while for optimal $T_{eg} = 1.8$ eV, m_S vs. Δ shows a gradual change across Δ_C . (e) In NiO, the m_S vs. Δ shows a nearly constant value for small $T_{eg} = 5$ meV, while for optimal $T_{eg} = 2.5$ eV, m_S vs. Δ shows a gradual change across Δ_C .

of the type $2p^6 3d^n \rightarrow 2p^5 3d^{n+1}$, $2p^6 3d^{n+1} \underline{L}^1 \rightarrow 2p^5 3d^{n+2} \underline{L}^1$, etc. From a careful check of the XAS spectrum, we try to decipher the role of the electronic parameters on the initial state multiplets of the d^n and $d^{n+1} \underline{L}^1$ states. In the following, we show that the actual transition to a negative charge-transfer character takes place when $\Delta_{eff} < 0$, and $d^{n+1} \underline{L}^1$ contribution dominates the initial state.

Fig. S9(a-c) shows the L -edge XAS spectra with a small $T_{eg} = 5$ meV and a small Gaussian broadening of 0.1 eV FWHM for selected Δ values, with all other parameters fixed to optimal values of CoTe₂. The spectra in panel(a) for $\Delta \leq \Delta_C = 0.25$ eV show hardly any change in the shape of the multiplet features but do show a systematic shift equal to the change in Δ . From Table VI, it is clear that all the spectra originate in the dominantly $d^{n+1} \underline{L}^1$ initial state multiplets. In panel (b), we plot two spectra for $\Delta > \Delta_C = 0.25$ eV and the results show very similar spectra but with significantly different multiplet features. From Table VI, we know that for $\Delta = 0.30$ eV, the initial state is dominated by the d^n state. This indicates the spectra in panel (b) originate in the d^n state and do not show a shift as is seen in Fig. S9(a) for $\Delta \leq \Delta_C$. In panel(c), we compare the spectra for $\Delta_C = 0.25$ eV with $\Delta = 0.30$ eV, and the spectrum $\Delta = 0.30$ eV calculated with 0.01 eV Gaussian broadening to see fine features. Panel (d) shows the same

spectra plotted on an expanded x-scale. The lowest energy multiplet of the $\Delta = 0.30$ eV spectrum is shifted 0.3 ± 0.1 eV below the lowest energy multiplet of the Δ_C spectrum. This difference of the spectral behavior for $\Delta \leq \Delta_C$ and $\Delta > \Delta_C$, together with the results of d^n count of Fig. 4(a) indicate that region A with $\Delta \leq \Delta_C = 0.25$ eV corresponds to the effective negative- Δ region, and region B with $\Delta > \Delta_C$ corresponds to an effective positive- Δ region.

In panels (e-f), a similar analysis was carried out for XAS spectra for $T_{eg} = 5$ meV and varying Δ , with all other parameters fixed to optimal values of NiTe₂. Panel (e) shows spectra for $\Delta \leq \Delta_C = -1.55$ eV. The spectra for $\Delta < \Delta_C$ show a sharp single peak and it shifts by an energy corresponding to the change in Δ . However, for Δ_C , the spectrum shows a sharp peak and a few very weak additional features at high energies. From Table VI, the spectrum for Δ_C is understood to originate from a dominantly $d^{n+1} \underline{L}^1$ initial state. But it shows a small admixture ($\sim 10\%$) of the d^n state. To confirm the origin of the weak features, panel (f) shows spectra for $\Delta > \Delta_C$, and all the spectra for $\Delta = -1.5$ to 0.0 exhibit the same spectral features with no shift. In panel (g), we compare the spectra for $\Delta_C = -1.55$ eV and $\Delta = -1.5$ eV but calculated with 0.01 eV Gaussian broadening to see fine features. The weak features in the spectrum for $\Delta_C = -1.55$ eV (plotted also on a 12 times

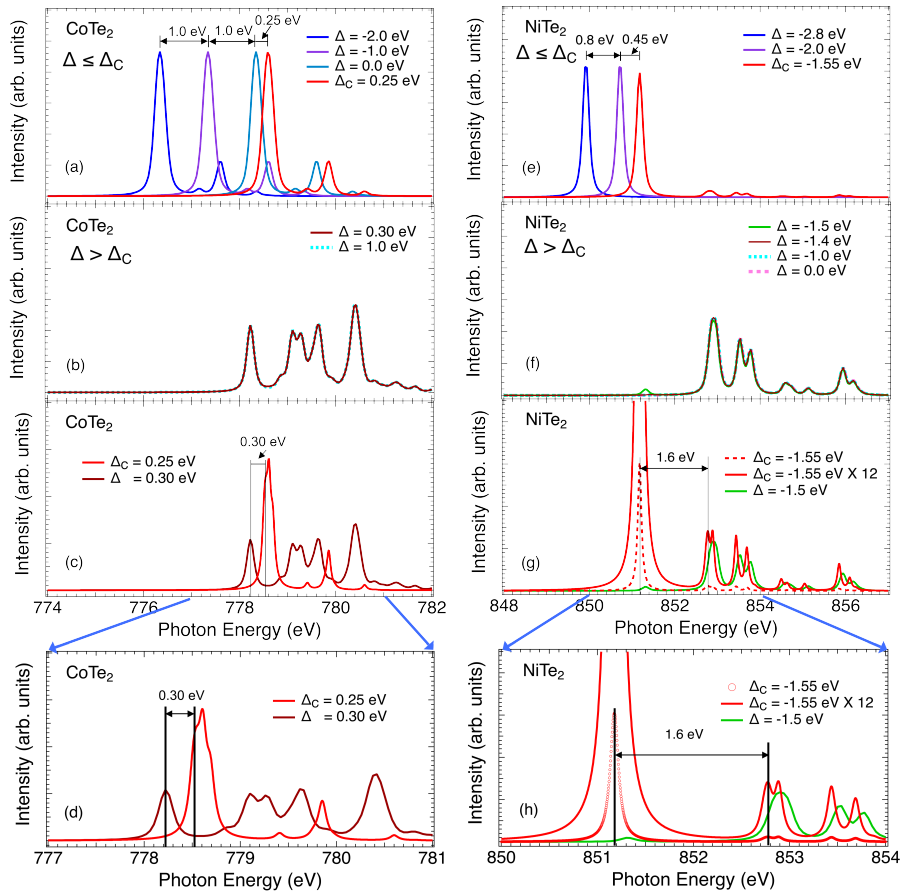


FIG. S9. (a-d) The XAS spectral calculations for $T_{eg} = 5$ meV and varying Δ with all other parameters fixed to optimal values of CoTe_2 : (a) for $\Delta \leq \Delta_C = 0.25$ eV, (b) for $\Delta > \Delta_C = 0.25$ eV. (c) for $\Delta = \Delta_C = 0.25$ eV ($d^{n+1}\underline{L}^1$ state) and $\Delta = 0.30$ eV (d^n state) (d) same as (c), but plotted on an expanded x-scale. (e-h) The XAS spectral calculations for $T_{eg} = 5$ meV and varying Δ with all other parameters fixed to optimal values of NiTe_2 : (e) for $\Delta \leq \Delta_C = -1.55$ eV, (f) for $\Delta > \Delta_C = -1.55$ eV (g) for $\Delta = \Delta_C = -1.55$ eV ($d^{n+1}\underline{L}^1$ state) and $\Delta = -1.5$ eV (d^n state) (h) same as (g), but plotted on an expanded x-scale.

expanded scale, red dashed line) show very similar features as seen in the spectrum for $\Delta = -1.5$ eV. For $\Delta = -1.5$ eV, Table VI confirms a dominant d^n character of the initial state and panel (f) shows that for $\Delta > \Delta_C$, all the spectra exhibit the same spectral features. Panel (h) shows the same spectra as in (g) but plotted on an expanded x-scale. It shows that the lowest energy multiplet of the $\Delta = -1.5$ eV spectrum is 1.6 ± 0.1 eV

above the lowest energy multiplet of the $\Delta_C = -1.55$ eV spectrum and implies that only when $\Delta \leq \Delta_C$, can we stabilize the negative charge-transfer $d^{n+1}\underline{L}^1$ dominant state with d^n -count of ~ 8 . Thus we can conclude that, together with the results of Fig. 4(b), region A corresponds to the effective negative- Δ region, and region B corresponds to an effective positive- Δ region.

- [R1] A. Prodan, F.W. Boswell., and J. M. Corbett, An Electron Microscopic Investigation of CoTe_2 Single Crystals, *Physica Status Solidi (a)* 36, K21 (1976).
 [R2] B. Ghosh, D. Mondal, C.-N. Kuo, C. S. Lue, J. Nayak, J. Fujii, I. Vobornik, A. Politano, and A. Agarwal, Observation of bulk states and spin-polarized topological surface states in transition metal dichalcogenide dirac semimetal candidate NiTe_2 , *Phys. Rev. B* 100, 195134 (2019).
 [R3] <https://www.topologicalquantumchemistry.com/>
 [R4] S. Jobic, R. Brec and J. Rouxel, Anionic Polymeric Bonds in Transition Metal Ditellurides, *Jl. Solid State Chem.* 96, 169

- (1992).
 [R5] W. Bensch, W. Heid, M. Muhler, S. Jobic, R. Brec, and J. Rouxel, Anionic polymeric bonds in nickel ditelluride: crystal structure, and experimental and theoretical band structure, *J. Solid State Chem.* 121, 87 (1996).
 [R6] R.D. Shannon, Revised effective ionic radii and systematic studies of interatomic distances in halides and chalcogenides, *Acta Cryst. A* 32, 751 (1976).
 [R7] M. W. Haverkort, M. Zwierzycki, and O. K. Andersen, Multiplet ligand-field theory using wannier orbitals, *Phys. Rev. B - Condens. Matter Mater. Phys.* 85, 165113 (2012).

- [R8] Y. Lu, M. Höppner, O. Gunnarsson, and M. W. Haverkort, Efficient real-frequency solver for dynamical mean-field theory, *Phys. Rev. B* 90, 085102 (2014).
- [R9] M. W. Haverkort, G. Sangiovanni, P. Hansmann, A. Toschi, Y. Lu, and S. Macke, Bands, resonances, edge singularities and excitons in core level spectroscopy investigated within the dynamical mean-field theory, *EPL* 108, 57004 (2014).
- [R10] F. De Groot, X-ray absorption and dichroism of transition metals and their compounds, *J. Electron Spectros. Relat. Phenomena* 67, 529 (1994).
- [R11] J. F. Moulder, W. F. Stickle, P. E. Sobol, and K. D. Bomben, *Handbook of X-ray Photoelectron Spectroscopy* (Perkin-Elmer Corporation, 1992).
- [R12] M. Trzhaskovskaya and V. Yarzhemsky, Dirac-Fock photoionization parameters for HAXPES applications, *At. Data Nucl. Data Tables* 119, 99 (2018).
- [R13] M. Muhler, W. Besch, and M. Schur, Preparation, crystal structures, experimental and theoretical electronic band structures of cobalt tellurides in the composition range $\text{CoTe}_{1.3}\text{-CoTe}_2$, *J. Phys. Condens. Matter.* 10, 2947 (1998).
- [R14] Z. Hu, L. Zhang, A. Chakraborty, G. D'Olimpio, J. Fujii, A. Ge, Y. Zhou, C. Liu, A. Agarwal, I. Vobornik and other, Terahertz nonlinear hall rectifiers based on spin-polarized topological electronic states in $1T\text{-CoTe}_2$, *Adv. Mater.* 35, 2209557 (2023).
- [R15] A complementary study on the experimental results for NiTe_2 is submitted to *Phys. Rev. B* as a regular article (available on arXiv at <http://arxiv.org/abs/2511.02245>).
- [R16] J. van Elp, J. L. Wieland, H. Eskes, P. Kuiper, G. A. Sawatzky, F. M. F. de Groot, and T. S. Turner, *Phys. Rev. B* 44, 6090 (1991).
- [R17] M. Ghiasi, A. Hariki, M. Winder, J. Kunes, A. Regoutz, T.-L. Lee, Y. Hu, J.-P. Rueff, and F. M. F. de Groot, *Phys. Rev. B* 100, 075146(2019).
- [R18] A. Chainani, T. Yokoya, Y. Takata, K. Tamasaku, M. Taguchi, T. Shimojima, N. Kamakura, K. Horiba, S. Tsuda, S. Shin, D. Miwa, Y. Nishino, T. Ishikawa, M. Yabashi, K. Kobayashi, H. Namatame, M. Taniguchi, K. Takada, T. Sasaki, H. Sakurai, and E. Takayama-Muromachi, Bulk electronic structure of $\text{Na}_{0.35}\text{CoO}_2 \cdot 3\text{H}_2\text{O}$, *Phys. Rev. B* 69, 180508(R)(2004).
- [R19] T. Mizokawa, A. Fujimori, T. Arima, Y. Tokura, N. Mori and J. Akimitsu, Electronic structure of PrNiO_3 studied by photoemission and x-ray-absorption spectroscopy: Band gap and orbital ordering, *Phys. Rev. B* 52, 13865 (1995).
- [R20] C. Piamonteze, F. M. F. de Groot, H. C. N. Tolentino, A. Y. Ramos, N. E. Massa, J. A. Alonso, and M. J. Martínez-Lope, Spin-orbit-induced mixed-spin ground state in RNiO_3 perovskites probed by x-ray absorption spectroscopy: Insight into the metal-to-insulator transition *Phys. Rev. B* 71, 020406 (2005).
- [R21] D. Meyers, S. Middey, M. Kareev, M. van Veenendaal, E. J. Moon, B. A. Gray, Jian Liu, J. W. Freeland, and J. Chakhalian, Strain-modulated Mott transition in EuNiO_3 ultrathin films *Phys. Rev. B* 88, 075116 (2013).
- [R22] R. J. Green, M. W. Haverkort, and G. A. Sawatzky, Bond disproportionation and dynamical charge fluctuations in the perovskite rare-earth nickelates, *Phys. Rev. B* 94, 195127 (2016).
- [R23] I. I. Mazin, D. I. Khomskii, R. Lengsdorf, J. A. Alonso, W. G. Marshall, R. M. Ibberson, A. Podlesnyak, M. J. Martínez-Lope, and M. M. Abd-Elmeguid, *Phys. Rev. Lett.* 98, 176406 (2007).
- [R24] H. Park, A. J. Millis, and C. A. Marianetti, *Phys. Rev. Lett.* 109, 156402 (2012).
- [R25] S. Johnston, A. Mukherjee, I. Elfimov, M. Berciu, and G. A. Sawatzky, Charge Disproportionation without Charge Transfer in the Rare-Earth-Element Nickelates as a Possible Mechanism for the Metal-Insulator Transition, *Phys. Rev. Lett.* 112, 106404 (2014).
- [R26] A. Subedi, O. E. Peil, and A. Georges, *Phys. Rev. B* 91, 075128 (2015).
- [R27] P. Seth, O. E. Peil, L. Pourovskii, M. Betzinger, C. Friedrich, O. Parcollet, S. Biermann, F. Aryasetiawan, and A. Georges, Renormalization of effective interactions in a negative charge transfer insulator, *Phys. Rev. B* 96, 205139 (2017).
- [R28] S. Biermann, F. Aryasetiawan and A. Georges, First-Principles Approach to the Electronic Structure of Strongly Correlated Systems: Combining the *GW* Approximation and Dynamical Mean-Field Theory, *Phys. Rev. Lett.* 90, 086402(2014).
- [R29] A. E. Bocquet, T. Saitoh, T. Mizokawa and A. Fujimori, Systematics in the electronic structure of 3d transition metal compounds, *Solid State Communications* 83, 11 (1992).
- [R30] A. Fujimori, A. E. Bocquet, T. Saitoh and T. Mizokawa, Electronic structure of 3d transition metal compounds: systematic chemical trends and multiplet effects, *Solid State Communications* 83, 11 (1992).
- [R31] A. Fujimori, Ligand Field and Charge Transfer in Transition metal compounds, *Jl. Phys. Soc. Jpn.* 93, 121002 (2024).